



Hepatotoxic and Neurotoxic Potential of Iron Oxide Nanoparticles in Wistar Rats: a Biochemical and Ultrastructural Study

Mostafa Mabrouk¹ · Ghadha Ibrahim Fouad² · Sara A. M. El-Sayed¹ · Maha Z. Rizk² · Hanan H. Beherei¹

Received: 19 July 2021 / Accepted: 27 September 2021 / Published online: 26 October 2021
© The Author(s), under exclusive licence to Springer Science+Business Media, LLC, part of Springer Nature 2021

Abstract

Iron oxide nanoparticles (IONPs) are increasingly being employed for in vivo biomedical nanotheranostic applications. The development of novel IONPs should be accompanied by careful scrutiny of their biocompatibility. Herein, we studied the effect of administration of three formulations of IONPs, based on their starting materials along with synthesizing methods, IONPs-chloride, IONPs-lactate, and IONPs-nitrate, on biochemical and ultrastructural aspects. Different techniques were utilized to assess the effect of different starting materials on the physical, morphological, chemical, surface area, magnetic, and particle size distribution accompanied with their surface charge properties. Their nanoscale sizes were below 40 nm and demonstrated surface up to 69m²/g, and increased magnetization of 71.273 emu/g. Moreover, we investigated the effects of an oral IONP administration (100 mg/kg/day) in rat for 14 days. The liver enzymatic functions were investigated. Liver and brain tissues were analyzed for oxidative stress. Finally, a transmission electron microscope (TEM) and inductively coupled plasma optical emission spectrometer (ICP-OES) were employed to investigate the ultrastructural alterations and to estimate content of iron in the selected tissues of IONP-exposed rats. This study showed that magnetite IONPs-chloride exhibited the safest toxicological profile and thus could be regarded as a promising nanotherapeutic candidate for brain or liver disorders.

Keywords Iron oxide nanoparticles · In vivo · Animal clinical observations · Nanotoxicity · Magnetite · Rats

Introduction

Nanoparticles (NPs) are defined as particles having at least one dimension ranging between 1 and 100 nm (< 100 nm) in diameter that can alter their physicochemical features in relevant to their original bulk material where their behavior relies upon their chemical composition and the size and/or shape of the particles [1, 2]. The European Commission's (EC) definition of nanomaterials (NMs) "EC NM Definition" states that "if 50% or more of the particles in a material have one or more of their external dimensions between 1 and

100 nm, the material is considered a nanomaterial" [3, 4]. NPs and submicron particles are defined as materials with "nano-metric" sizes (1–100 and 100–1000 nm, respectively) that interact with biological systems in an irregular manner due to their high surface to volume ratio [5]. NPs have been employed in several fields of technology due to their physicochemical features including small size, large surface area, high surface to mass ratio, as well as in vivo drug delivery characteristics [6, 7]. Nanotechnology has been demonstrated to be beneficial for several medical applications including drug delivery and the development of nanoscale materials for medical applications, through controlling the material features at the nanometer scale either by scaling up from a single collection of NPs or by refining bulk (parent) materials into a required nanoscale [8]. NPs helped to overcome drug resistance in some neurodegenerative disorders through enabling delivery of therapeutic agents across the barriers such as the blood–brain barrier (BBB) [9].

The combination of diagnosis and therapy in a single platform, known as "theranostics," can work synergistically to improve all phases of patient care, from disease prognosis and diagnosis to therapeutics option [10, 11].

Mostafa Mabrouk and Ghadha Ibrahim Fouad are contributed equally to this work

✉ Ghadha Ibrahim Fouad
ghadhaibrahim@yahoo.com; gi.fouad@nrc.sci.eg

¹ Refractories, Ceramics and Building Materials Department, National Research Centre, 33 El Bohouth St, PO Box 12622, Dokki, Cairo, Egypt

² Department of Therapeutic Chemistry, National Research Centre, 33 El-Bohouth St, 12622, Dokki, Cairo, Egypt

Nanotheranostics (*i.e.*, theranostic nanomedicines) integrates the simultaneous non-invasive “in vivo” targeting, diagnosis, and treatment of diseases with the potential to track simultaneous drug release and biodistribution, thus predicting and validating the effectiveness of the therapy and therefore performing a real personalized and optimized medicine [12]. Nanotheranostic-based approaches could provide a novel platform for the development of nanotherapeutic and nanodiagnostic agents for several disorders through saving time and money *via* integration of therapeutic and diagnostic (*e.g.*, bioimaging) functionalities in a single platform, generating a “smart” multifunctional strategy for disease management [13], that is capable of targeting affected “non-healthy” tissues through improving drug delivery across various physiological barriers, and providing data on the stage of the disease, and even on the therapy response and effectiveness in real time [14].

Therefore, an “ideal nanotheranostic agent” should circulate for a long time in the blood and demonstrate a good release behavior, effective tissue-target specificity and penetration, bioimaging possibility, and high target to background ratio [15]. Several nanotheranostic agents demonstrated the potential to localize diagnostic and therapeutic agents in specific affected regions and decrease side effects [16]. Nanotheranostics are approaches based on carriers of submicron or nanosizes [16]; therefore, the specific physicochemical features of the nanotheranostics would directly affect the biodistribution, cellular uptake, and blood half-life of NPs [17]. In other words, the dose and the frequency of administration of nanoparticles would affect their “in vivo” destiny; for example, nanodiagnostic-used iron oxide NPs “IONPs” should be administered once or at least with a longer spacing interval as compared to clinically nanotheranostic-used IONPs [12]. Accordingly, nanotheranostic-based approaches demonstrated a promising application in diagnostics and non-invasive therapy of several diseases through providing both nanodiagnostic agents enabling early detection of diseases, as well as nanotherapeutic strategy facilitating delivery of nano-drugs to target tissues; for instance, there is a great unmet need for novel therapeutic options for cancer as several cancer patients encounter adverse effects due to “off-target” cytotoxicity and drug interaction with biological molecules [18]; therefore, nanotheranostic-based approaches provided significant benefits in the management of disorders including cancer, neurodegenerative disorders, and cardiovascular diseases [19–21].

Currently, there are about 2000 NP-containing products have become available in the market [7]. The absolute diversity of the physicochemical features of NPs also develops research questions regarding their toxic effects [9, 22]. Thereby, it is mandatory to determine the interactions of NPs with cells and biomolecules [23, 24]. This leads to the emergence of the field of “Nanotoxicology”

that aimed at demonstrating data regarding the nanotoxicity potential and the biochemical and structural alterations in vivo [25], due to the potential of deposition of stable NPs and subsequent induced nanotoxicity [26]. Several studies investigated in vivo nanotoxicity in different organs [27–29]. Actually, the current knowledge about the biocompatibility and bioreactivity of NPs is limited [30]. Therefore, there is a keen interest to understand the interaction between NPs and biological systems.

Iron is an abundant element that could be utilized in several biomedical applications; in addition, there is a keen interest in ferro- and ferri- magnetic materials for nanotheranostics including targeting, tracking, and imaging [31]. Iron oxide nanoparticles (IONPs) have promising characteristics such as magnetic behavior and biocompatibility owed to its large surface area along with functionalization suitability to a large number of functional groups that enable IONP cross-linking to small molecules for nanodiagnostics (*e.g.*, imaging) or nanotherapeutics (*e.g.*, delivery of therapeutic agents) [32]; moreover, IONPs have been found to be relatively not toxic [33]. Therefore, IONPs are regarded as ideal nanotheranostic agents. There are several biomedical applications of IONPs including their use as contrasting agents (CA) for magnetic resonance imaging (MRI), carriers for drug delivery, tissue engineering, cell-labeling, enzyme-immobilization, protein-purification, magnetic hyperthermia, and bio-sensing [34–38]. Moreover, IONPs, under an external magnetic field, are capable of targeting a certain location within the body [39] and can cross BBB [40]. Several factors should be considered for biomedical applications of IONPs including size, surface charge, lipophilicity, and serum half-life, and BBB penetration [41].

Synthesis of NPs with a magnetic property, such as IONPs, has attracted attention in the last few years because of their unique physicochemical features [42]. Although there are a variety of magnetic materials such as iron oxide, metal ferrite, alloys, nickel, and cobalt [43], magnetite Fe_3O_4 is the most widely used one in many fields due to its chemical stability, super paramagnetic property [44], high biocompatibility [45], non-toxicity [46], inertness, and ease of detection in the human body [47]. The most used magnetic nanomaterial as a nanocarrier is the magnetite Fe_3O_4 due to its fine size and biocompatibility [48]. IONPs are employed in biomedicine as the least hazardous among metallic NPs [49, 50]; this might be attributed to the limited biodistribution of IONPs as they are subjected to body’s highly active clearance mechanism [41, 51]. The bioavailability of IONPs in biological applications is improved by the current advancement in synthesis, characterization, and surface modification of NPs [52]. IONPs have also been found to be transported to the brain in different animal models [53]. Therefore, IONPs might represent a good candidate for a

plethora of applications in the central nervous system (CNS) disorders [54, 55].

There are conflicting studies regarding the cytotoxicity of IONPs; some studies have showed the high biocompatibility and none-to-low toxicity of IONPs [33, 56–59]. Other contradicting studies reported that IONPs might trigger genotoxicity, biochemical alterations, and oxidative stress [26, 27, 53, 60]. IONP-induced oxidative stress might be ascribed to a large surface area presented by NPs for redox cycling; in addition, using enzymatic activity to separate iron ions from their surface may also generate ROS [46]. Released iron ions from IONPs can contribute to Fenton's reaction, generate ROS from H_2O_2 and superoxide, accumulate in the tissue, and finally leading to damage of macromolecules [61].

Keeping in mind that nanomedicine is aimed at designing and developing non-toxic, biocompatible, and multi-functional nano-formulation. Accordingly, the application of IONPs in the neurodegenerative disorders and cancer needs serious caution [38, 62]. With the increasing production and use of these IONPs, there is an evident higher risk of adverse outcomes for the environment and humans. Therefore, the physicochemical features (*e.g.*, size, shape, chemical functionality, surface coating or surface charge, and the type of coating and side groups) of IONPs could be effectively tuned to control their biological and magnetic behavior [58]. Creating toxicological profile of IONPs could help overcoming their potential nanotoxicity.

The main goal of this research is to develop novel IONPs which could be used in medical applications as nanotherapeutic agents. This research is aimed at comparing the *in vivo* toxicity of three different formulations of IONPs including ferric chloride ($FeCl_3$), ferric lactate ($C_9H_{18}FeO_9$), and ferric nitrate $Fe(NO_3)_3$. Evaluating their potential to induce oxidative stress and to cause ultrastructural alterations in the liver and brain of rats, after oral administration for 14 days, was also assessed. Special emphasis was on the effects of the liver and the brain as the safest formulation of IONPs is aimed to be used as a drug delivery system. For this purpose, porous IONPs were synthesized by using solvothermal method using different iron precursors. This was followed by assessing their physical, morphological, chemical, surface area, magnetic, and particle size distribution accompanied with their surface charges properties.

Materials and Methods

Materials

The anhydrous iron chloride ($FeCl_3$) (97%) (MWt=162.20 g/mol), iron nitrate nonahydrate ($Fe(NO_3)_3 \cdot 9H_2O$) ($\geq 98\%$) (MWt=404.00 g/mol), and iron lactate hydrate ($Fe(C_3H_5O_3)_2$) ($\geq 98\%$) (MWt=233.99 g/mol)

were purchased from Sigma-Aldrich (Germany). Ethylene glycol ($(CH_2OH)_2$) (99%) (MWt=62.07 g/mol) was purchased from Alpha (India). Hydrated hydrazine ($N_2H_4 \cdot H_2O$) (99%) (MWt=50.06 g/mol) was purchased from Advent (India). Absolute ethanol (C_2H_5O) (99.8%) (MWt=46.07 g/mol) was purchased from Piochem (Egypt).

Methods

Preparation of IONPs

Method I (IO1) This method of preparation is considered a modification method of a previous research [44]. Firstly, anhydrous iron chloride was dissolved in 60 mL of ethylene glycol (EG) that the mixture was stirred at room temperature until a yellowish brown suspension was obtained. Then, 6 mL of hydrated hydrazine was added to the prepared solution that resulted in a brown solution. Stirring the mixture at room temperature till obtain a yellowish brown suspension. The suspension was transferred into a Teflon-lined stainless-steel autoclave (80 mL) and the autoclave was put in the dryer at 200 °C for 2 days. Afterword, allow the temperature of the autoclave to reach room temperature. The formed mixture was centrifuged under the following conditions: 7000 rpm, 15 min, 20 °C and washed with distilled water and absolute ethanol several times to collect the black precipitate. The black precipitate was then dried at 37 °C for 2 days.

Method II (IO2) Iron nitrate precursor was utilized in this method as mentioned before in a previous research [63] including several modifications. First, dissolve 1 g of $Fe(NO_3)_3 \cdot 9H_2O$ in 200 mL EG stirring at 40 °C for 2 h. Afterword, the prepared solution was put in the dryer at 80 °C until precipitation; then, the temperature was increased to 200 °C for another 2 days. After cooled to room temperature, the product was collected by centrifugation (7000 rpm, 15 min, 20 °C) and washed with distilled water and absolute ethanol several times. Then, the product was dried at 60 °C for 2 days.

Method III (IO3) The second method was repeated and iron nitrate was replaced with iron lactate. The prepared iron nanoparticles were numbered for simplicity as listed in Table 1.

Table 1 Codes of the prepared iron oxides

Code	Sample name
IO1	Magnetic iron (I) oxide using iron chloride (Fe_3O_4)
IO2	Iron (II) oxide using iron nitrate (Fe_2O_3)
IO3	Iron (III) oxide using iron lactate (Fe_2O_3)

Material Characterizations

XRD Analysis

The X-ray diffraction (XRD) technique was employed to determine the crystallinity/amorphous nature of the IONPs. The test was conducted using model BRUKUR (Discover-D8, USA).

TEM Analysis

Particle size of the prepared IONPs was analyzed using Transmission Electron Microscopy (TEM) (JEOL, Japan, JEM-2100, ELECTRON MICROSCPE, TEM-HR). A trace amount of iron oxides was dispersed in ethanol, then few 5 μ L of the solution was dropped on a copper grid and images were further recorded by TEM.

FTIR Analysis

In order to know the formed functional groups of the prepared iron oxides, infrared spectra were obtained using Fourier Transformer Infrared (FTIR) spectrophotometer (model FT/IR-6100 type A). The spectra were recorded at a wave number range of 400–4000 cm^{-1} . The measured samples were prepared by mixing iron oxide powders with KBr.

Surface Area

Nitrogen adsorption–desorption measurements were carried out at 77.35 K on a Nova Touch LX4 (Quantachrome, USA) to determine the Brunauer–Emmett–Teller (BET) surface area and complete isotherm. Before measurements, samples were degassed under high vacuum for a specific time. Liquid nitrogen was used to cool samples and analyzed by measuring the volume of (N_2) gas adsorbed at specific pressures. The samples (100 mg) of the magnetite powders were exposed to two phases of examination: first, following a degassing stage at -196 °C for 3 h and, also, a nitrogen intrusion and desorption combined stage for precise examination of the surface area. The pore volume was measured from the adsorption branch of the isotherm curve at $P/P_0=0.995$ assuming complete pore saturation using BJH method.

Magnetic Properties

To detect the magnetic properties of the prepared iron oxides (IO1, IO2, and IO3), a vibrating sample magnetometer

(VSM, Lake Shore Model 7410, USA) was used with an applied field 31 kOe.

Particle Size Distribution and Zeta Potential

The size distribution and the zeta potential of the prepared iron oxides (IO1, IO2, and IO3) were determined using the method of light scattering using Zetasizer Nano ZS instrument (Malvern Instruments, UK accessorized with a 633 nm laser). Samples were dispersed in a clear disposable zeta cell by using deionized water at 25 °C. Measuring position in case of measuring the size distribution is 5.50 mm from the wall of Zeta cuvette and 2.00 mm in case of measuring the zeta potential. Malvern instrument's dispersion technology software (Version 7.13) was used for data analysis and zeta potential.

In vivo studies

Animals

Twenty-four female albino Wistar rats were sourced from the Animal House of the National Research Centre (Dokki, Giza, Egypt). The rats obtained were 6–8 weeks old and weighed 150 ± 25 g. Before the experimental period, the animals were allowed to acclimatize for 2 weeks in polypropylene cages (six per group). The animals were fed standard laboratory pellets with water ad libitum and the floors of the cages were covered with wood shavings, which were replaced every 3 days. They were maintained under standard conditions of automated light cycles (12 h light/12 h dark), humidity (55–65%), and temperature (22 ± 3 °C).

All experimental procedures were performed in compliance with the ARRIVE guidelines and with the European Council Directive 2010/63/EU on the care and use of laboratory animal. All animals' procedures were carried out in accordance with the Ethical Committee, National Research Centre (NRC), Egypt (**Approval no. 19–313**). All animals used in this research were treated humanely according to the institutional guidelines, with due consideration for the alleviation of distress and discomfort. Getting rid of the animals after termination was done rapidly by the aid of the Safety and Health Committee, NRC, Egypt.

Experimental Design

Acute Oral Toxicity Study

An in vivo oral toxicity study was performed according to the Organization of Economic Co-operation and Development (OECD) guideline 420 for testing a chemical [64]. For oral administration, IONPs (in powder form) were suspended in polyethylene glycol (PG) (Fig. 1) immediately

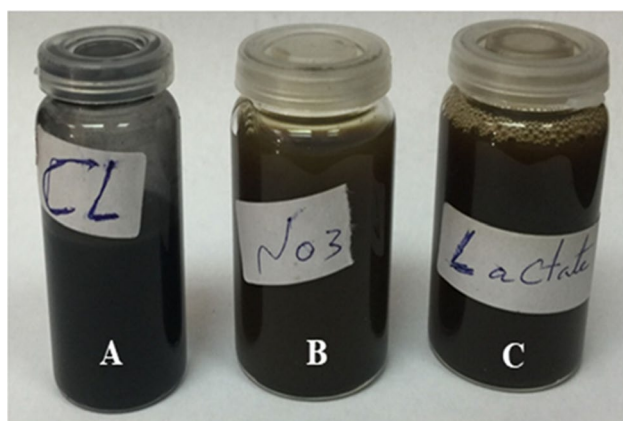


Fig. 1 Three formulations of IONPs dispersed in polyethylene glycol (PG) to be administrated to rats: (A) IONPs-chloride (IO1), (B) IONPs-nitrate (IO2), and (C) IONPs-lactate (IO3). *Preference for color: online*

Table 2 The different experimental groups

Groups	Administrations
Group 1	Negative control received PG (vehicle control)
Group 2	IONPs-lactate (IO3)
Group 3	IONPs-nitrate (IO2)
Group 4	IONPs-chloride (IO1)

before administration. Before each administration, the solution was also vortexed for 1 min to prevent probable agglomeration of IONPs. The three formulations of IONPs were administrated orally at a daily dose for a period of 14 days. Figure 1 shows the different forms of administrated IONPs (IO1-IO2-IO3). Following 2 weeks of acclimatization, rats were randomly divided into four groups including six rats each:

Three groups were administrated 100 mg/kg/day of the different IONPs prepared in this study orally once a day for 14 days. The selected doses of IONPs in animal studies were chosen according to the previous studies by Najafabadi et al. [65] and Askri et al. [66]. The IONP-exposed rats were compared with control group that was administrated 100 mg/kg/day of PG at the same conditions as listed in Table 2.

Toxicity Analysis

Body Weight Measurement

The body weight of the animals was recorded regularly (twice a week) throughout the experimental period.

Observation of Clinical Signs of Stress and Neurotoxicity

Body weights of all the animals were recorded regularly throughout the experimental period and on the day of sacrifice. Home cage observations of the animals were carried out regularly (twice a week until the completion of experiment) in order to analyze clinical signs of stress and neurotoxicity including toxicity-induced unusual behaviors like movement (spinning, convulsions, decreased physical activities), anxiety, lethargy, appearance (e.g., ruffled skin coat), and mortality.

Blood Collection and Tissue Sampling

Collection of Blood Samples

Five days after administration of the last dose, rats were fasted overnight, with free access to water; blood samples were collected from all groups just before sacrificing the rats, under light anesthesia with diethyl ether. The blood was collected, before decapitation, from the sublingual vein of random rats in each group. The blood samples were left to clot in clean, dry test tubes for 30 min at room temperature (RT) and then centrifuged at 4000 RPM for 15 min, which were performed with SIGMA centrifuge (3-18KS, Germany). The clear supernatant serum was then frozen at $-20\text{ }^{\circ}\text{C}$ for biochemical analyses of aspartate amino transaminase (AST), alanine amino transaminase (ALT), and alkaline phosphatase (ALP). All measurements were performed according to the procedures of the biochemical kit assay.

Brain and Liver Tissues Sampling and Preparation

After the rats were anesthetized and decapitated, the head was moved onto the dry ice for 4 min. The whole brain was rapidly dissected on an ice-cooled glass plate, thoroughly washed with isotonic saline, dried on a filter paper, and sagittally divided into two portions. The same procedure was performed for liver tissues. Small portions (0.5 g) of the brain or liver were homogenized using an electrical homogenizer (Remi 8000 RPM), to give 10% (w/v) homogenate in ice-cold medium in 9 volumes ($1:9\ w/v$) of a 50 mM phosphate-buffered saline (PBS) pH 7.4 containing 0.1 mmol/L ethylene-diamine-tetra-acetic acid (EDTA). The unbroken cells and cell debris were removed by centrifugation at 4000 RPM for 30 min at $4\text{ }^{\circ}\text{C}$ to prepare 10% supernatants. Following protocol procedures, the clear supernatant was analyzed to determine the levels of catalase (CAT) activity, malondialdehyde (MDA), and reduced glutathione (GSH) contents, following the protocols. Another portion of brain and liver tissues was utilized by inductively coupled plasma atomic emission spectroscopy (ICP-OES). Small fragments

of the brain (either right or left) and liver was used for ultrastructural evaluation using transmission electron microscope (TEM).

Biochemical Assays

Biochemical determinations in rat serum and tissue homogenates were carried out on a UV/Vis Spectrophotometer (Agilent Technologies, India).

Measurement of Liver Function Markers

Serum samples were used for colorimetric determinations of the enzymatic activities of AST and ALT according to Reitman and Frankel [67], and ALP according to Belfield and Goldberg [68], using kits from Biodiagnostic Co., Egypt. Enzyme activities of AST and ALT were expressed as Units (U)/mL, where ALP activities were expressed as IU/L.

Assessment of Oxidative Stress Markers in the Liver and the Brain

Lipid Peroxidation (LPO)

Lipid peroxidation was estimated colorimetrically, using kits from Biodiagnostic Co., Egypt, according to the protocol proposed by Ohkawa et al. [69]. Lipid peroxidation levels were estimated *via* measuring thiobarbituric acid reactive substances (TBARS) as malondialdehyde (MDA), a product of lipid peroxidation. The reaction between thiobarbituric acid and MDA, in acidic medium, resulted in pink-colored product that was measured spectrophotometrically at 534 nm. The results were expressed as nmol/g tissue.

Reduced Glutathione Content

GSH content was measured colorimetrically, using kits from Biodiagnostic, Egypt, according to the method reported by Beutler et al. [70] and it involved the spectrophotometric detection of yellow-colored product formed as a result of the reduction of 5,5-dithiobis-2-nitrobenzoic acid (DTNB) by GSH. The absorbance of the sample was obtained at 405 nm. The results were expressed as mg/g tissue.

Assay of Catalase Activity

Measurement of antioxidant catalase (CAT) enzyme activity was measured colorimetrically, using kits from Biodiagnostic, Egypt, according to Aebi [71]. The reaction mixture was prepared with 0.5 mL of 10 mM PBS (pH 7.0) and 0.4 mL of 0.2 M H₂O₂. One hundred microliters of tissue homogenate was added to the reaction mixture. Then, the mixture was immediately vortexed and incubated for 1 min at 37 °C.

Each unit of catalase decomposes 1 μM of H₂O₂ per minute. The absorbance of sample was obtained at 510 nm. Catalase activity was expressed as Units/g.

Hepatic and Brain Uptake of IONPs

At the end of the exposure phase, collected liver and brain tissues were stored at -80 °C until utilized by ICP-OES to quantify iron (Fe) content at alternate wavelengths (232 nm and 238 nm). Briefly, 0.5–1 g liver or brain tissue was digested in an acid solution using *Anton-Paar microwave digestion system* (Multiwave PRO) using 5 mL of 65% concentrated nitric acid (conc. HNO₃) as acid reagent [72]. All samples were analyzed as triplicates for quantification of Fe. The determination of Fe content was analyzed using the Agilent 5100 Synchronous Vertical Dual View (SVDV) ICP-OES, with Agilent Vapor Generation Accessory VGA 77. Accuracy and precision of the iron ion measurements were confirmed using external reference standards from Merck, and standard reference material and quality control sample from National Institute of Standards and Technology (NIST) were used to confirm the instrument reading.

Ultrastructural Analysis Using a Transmission Electron Microscopy

Brains/livers from four random rats of each experimental group were randomly collected for TEM examination. Brain and liver tissues were cut into small fragments (small blocks of about 1 mm³), immediately fixed in ice-cold Karnovsky's fixative (2.5% glutaraldehyde + 4% paraformaldehyde + 0.1 M phosphate buffer), for 4 h at RT, incubated at 4 °C overnight, and washed with PBS. Tissues were maintained in 1% osmium tetra-oxide for 1 h post-fixation. After washing in PBS, tissues were sequentially dehydrated in ascending grades of alcohol solutions (50%, 70%, 80%, 95%, and 100%). Further treatment of tissue with propylene oxide (30 min), propylene oxide-resin (overnight), and pure resin was conducted for 48 h. Thereafter, tissues were embedded in Better Equipment for Electron Microscopy (BEEM) capsules. Ultrathin sections stained with uranyl-acetate and lead citrate were examined under a TEM (JEOL, Japan, JEM-2100, ELECTRON MICROSCOPE, TEM-HR) [73].

Statistical Analysis

The results of this study are expressed as mean values ± standard error of the mean (SEM) for *n* = 6 rats per group. For statistical analysis, one-way analysis of variance (ANOVA) followed by Tukey's test as the post hoc analysis was performed using the SPSS statistical software version

16. A value of $p < 0.05$ was considered to be statistically significant.

Results

XRD Analysis

XRD analysis is carried out to show the sharp and the intense peaks that reveal the formation of the Fe_3O_4 crystalline sample. Figure 2 shows the diffraction peaks of (IO1) locating at $2\theta = 30.1, 35.8, 43.1, 53.8, 57.3,$ and 63.0° can be indexed to (220), (311), (400), (422), (511), and (440) planes of Fe_3O_4 (JCPDS card no. 19–629), respectively [42, 43, 63].

TEM Analysis

To confirm the formation iron oxides nanospheres, TEM analysis was performed with different magnifications to evaluate the effect of the starting materials and method on their final morphology features. TEM images (Fig. 3) show that IO1 has nanosphere particles of approximately ≈ 20 nm and IO2 has nanosized particles of 5–7 nm. In addition to the NPs of IO3 that demonstrated diameter range between 32 and 40 nm, the pattern of diffraction showed that the formed Fe_3O_4 (IO1) particles are found in single crystal-like electron diffraction pattern not polycrystals, as there are no aggregates of nanocrystallites; the particles are found in individual Fe_3O_4 particle [42, 44]. While in the case of the amorphous Fe_2O_3 , the electron diffraction reveals the porous structure of the prepared NPs.

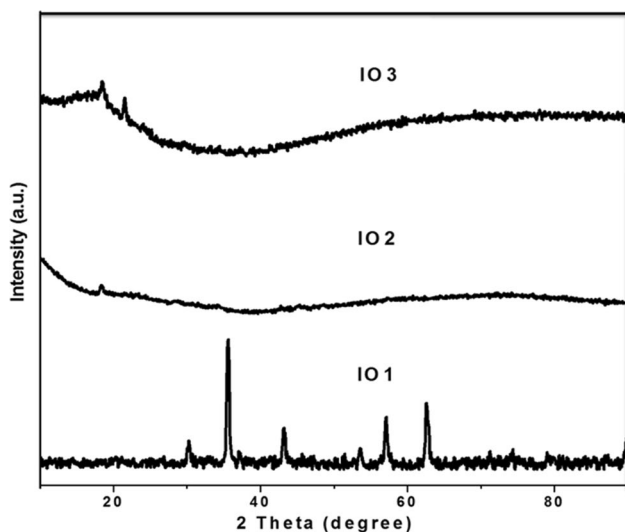


Fig. 2 XRD patterns of the prepared iron oxides: IO1, IO2, and IO3

FTIR Analysis

FTIR spectrum of the prepared iron oxides is shown in Fig. 4. The strong and the broad band at 588, 603, and 607 cm^{-1} for IO1, IO2, and IO3, respectively, is corresponding to Fe–O bond vibration modes, which was the characteristic absorption peak of magnetite Fe_3O_4 and hematite Fe_2O_3 [72, 73]. Bands at 1049, 1164, and 1054 cm^{-1} for IO1, IO2, and IO3, respectively, are attributed to C–O stretching of alcoholic derivatives [74]. In each spectrum, the sharp band at 1384 cm^{-1} is corresponding to bending C–H. The strong band of the bending O–H group at all spectra at 1617 cm^{-1} is due to the presence of ethylene glycol as a precursor. IO1, IO2, and IO3 have bands at 2923, 2927, and 2925 cm^{-1} that is due to C–H stretching bands. The strong broad bands at 3473, 3478, and 3473 cm^{-1} for IO1, IO2, and IO3 are attributed to stretching O–H due to the presence of alcoholic group (ethylene glycol) [74]. This implies that the influence of the starting materials and synthesizing method is ignored on their functional groups.

Surface Area

The surface area of the material is an important parameter that greatly correlates to the degree of the active sites (reactivity) of the material. BET surface area, pore volume, and average pore radius of the prepared iron oxide nanoparticles are determined and recorded in Table 3. The BET surface area of IO1, IO2, and IO3 is 69.8727, 33.9421, and 36.1064, respectively. This result showed that IO1 has the larger surface area and pore volume and the smallest pore radius. Figure 5 shows N_2 adsorption–desorption isotherms of IO1, IO2, and IO3.

The average pore diameter and pore volume were slightly changed with changing the starting material of the IONPs. From the cumulative pore volume observed, range of pore radius for IONPs was 3–20 nm (IO1) and 3–10 nm (IO2 and IO3). Their isotherms demonstrated minor changes with changing the precursor. The resulting isotherm curves for all samples exhibit hysteresis behavior with two branches, adsorption (capillary condensation) and desorption (evaporation), indicating the existence of open pores between its particles, according to IUPAC classification [75].

Figure 5(a, c) shows that the hysteresis lope of samples IO1 and IO2 matched that of a type II hysteresis loop. The adsorption increased dramatically at low relative pressures, suggesting the existence of micropore structure. The monolayer adsorption converted to multilayer adsorption as the pressure increased, and because of the well-developed macropore, the adsorbance dramatically increased when the relative pressure becomes 1. Furthermore, as is typical with open wedge pores, the maximum absorbance for the adsorption and desorption branches of type H3 was not detected.

Fig. 3 TEM images of the prepared iron oxides: IO1, IO2, and IO3. Preference for color: online

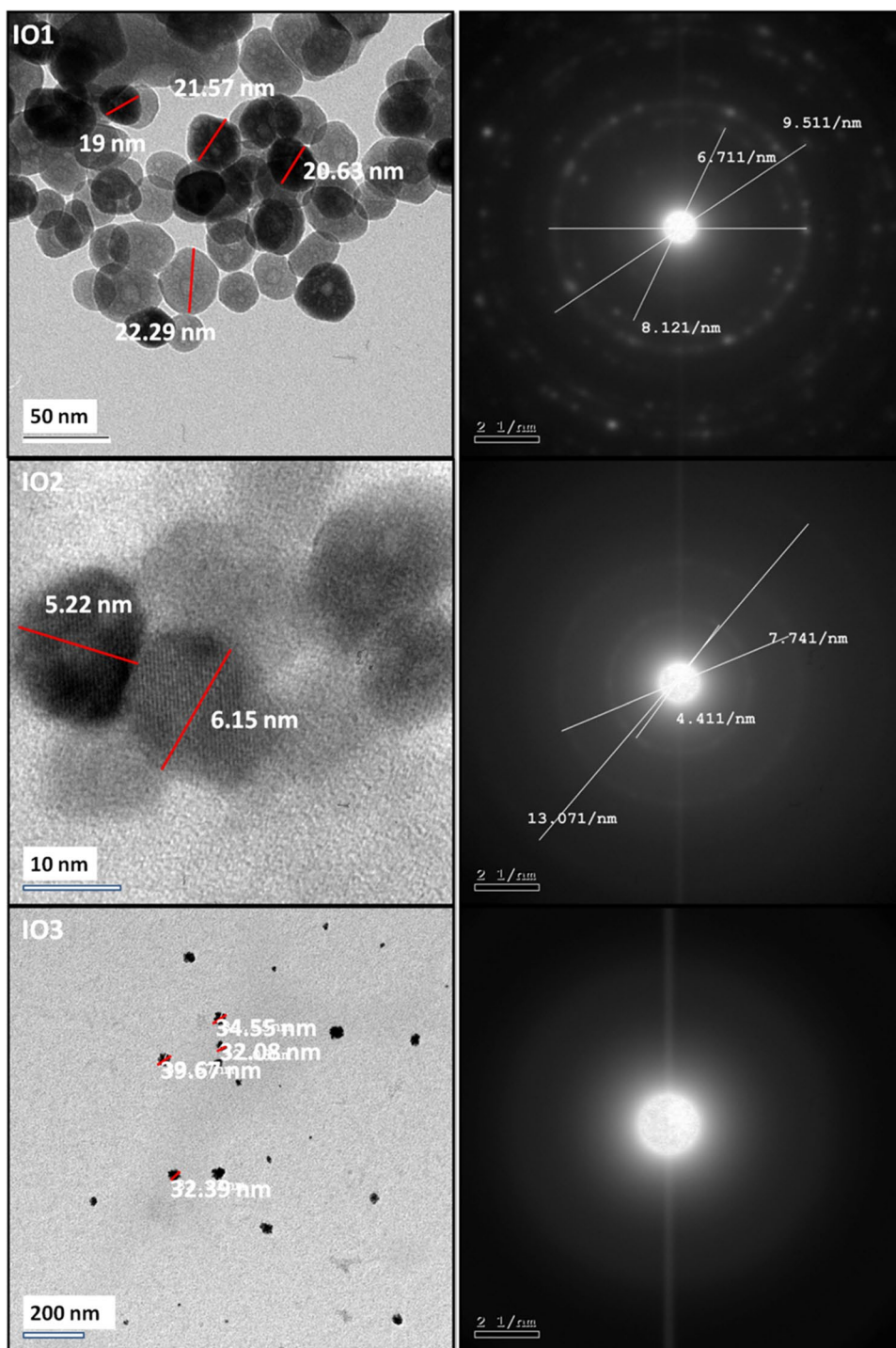


Figure 5(e) sample IO3 shows open isotherm, which indicates that the volumes adsorbed are so small, adsorption kinetics can become apparent, and large massive particles do not encourage rapid equilibrium. When completely equilibrated, however, the isotherm assumes a type II non-porous material characteristic and thus a pore size distribution. This was also in agreement with the results of pore volume distributions of IO1, IO2 and IO3 that are represented in

Fig. 5(b, d, f), respectively. This was also in agreement with the results of pore volume distributions of IO1, IO2 and IO3 that are represented in Fig. 5(b, d, f), respectively.

Magnetic Properties

The superparamagnetic property is an essential characteristic for the biomedical applications especially drug delivery,

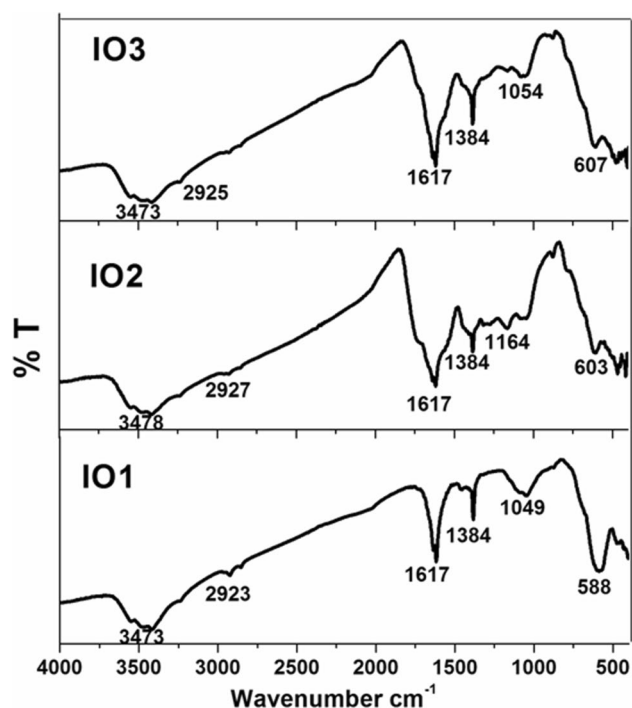


Fig. 4 FTIR spectra of the prepared iron oxides: IO1, IO2, and IO3

Table 3 Pore structure parameters of the prepared samples

Samples	BET surface (m ² /g)	Pore volume (cm ³ /g)	Average pore radius (nm)
IO1	69.8727 ± 3.5	0.146743 ± 0.010	1.9516e ⁺⁰⁰¹
IO2	33.9421 ± 1.2	0.0263579 ± 0.006	4.0175e ⁺⁰⁰¹
IO3	36.1064 ± 1.7	0.0333718 ± 0.004	3.7767e ⁺⁰⁰¹

and Fe₃O₄ nanoparticle acts as a single magnetic domain, at temperatures above the blocking temperature [76, 77]. Vibrating sample magnetometer (VSM) was performed to characterize the hysteresis loops of IONPs as a function of the magnetic field at room temperature (Fig. 6). The values of saturation magnetization (M_s) and high coercivity (H_{ci}) are shown in Table 4. The saturation magnetization of IO1 was about 71.273 emu/g that is compatible with that found for Fe₃O₄ magnetite [78, 79], compared to 0.354 emu/g and 0.509 emu/g for IO2 and IO3, respectively. VSM test indicates that IO1 has superparamagnetic nature can be easily separated from solution using magnetic field that revealed IO1 is a Fe₃O₄ phase. However, IO2 and IO3 samples show weak ferromagnetic behavior of the sample that explained the amorphous Fe₂O₃ hematite phase [80, 81]. It is highly worth the increasing of the particle size affects the M_s value obtained by applying the law of approach to saturation [82].

Particle Size Distribution and Zeta Potential

To know the particle size distribution and charges of the fabricated IONPs that governs the cell interaction with nanoparticles, size distribution and zeta potential were carried out using Zetasizer instrument. Figure 7 shows the particle size distribution of IO1, IO2, and IO3. IONPs exhibited an average dynamic distribution of particle diameters of 1000, 1847, and 612.4 nm in 100%, respectively.

Zeta potential (Fig. 8) of IO1, IO2, and IO3 nanoparticles has a maximum zeta potential value at −14.5, −5.95, −21.9 mV, respectively. The noted variation of the particle nanosize between TEM and the zetasizer might be attributed to the agglomeration in nanoscale of nano-powders [83, 84].

Clinical Sign Observation and Body Weight Change

Following exposure to IONPs, the clinical and behavioral (neurotoxic) signs, in addition to other toxicity signs including appearance, hair, possible trauma, and mortality, were carefully monitored. Variations in clinical sign parameters were observed throughout the experimental period from day 0 to day 19 (the day of animal euthanasia).

Treatment with a dose of 100 mg/kg body weight was well tolerated by the animal group treated with IO1; the rats did not show any sign of mortality or exposure-related abnormalities throughout the observation period, compared to groups treated with IO2 and IO3 nanoparticles; thus, no clinical symptom was observed in the control and IO1 groups. Groups treated with IO2 and IO3 nanoparticles exhibited a clear toxicological profile; they demonstrated clinical signs of general toxicity related to appearance (including ruffled skin coat, in addition to loss of hair and fluid accumulation at the abdominal area) and unusual behavior (including lethargy, ataxia, and decreased physical activities). In addition, difficulty in blood collection was experienced in rats exposed to IO2 and IO3. Hence, it was concluded that the formulated IO1 was found to be orally safe at a dose of 100 mg/kg body weight.

Regarding body weights of rats exposed to IONPs, the oral administration of IONPs to rats for 14 days altered the average body weights relative to the control (Fig. 9). Body weight change, as important toxicity index, was measured twice a week. Body weight of the animals decreased significantly from day 0 to 4, then it showed a constant increase from days 4 to 8, finally body weight from 8 to 14 days was constantly declined. This style of fluctuation was observed in all the experimental groups but with different degrees. As compared to the initial body weights records, negative control rats exhibited a significant decrease by 10.59%; on the other side, rats of IO3 and IO1 groups demonstrated a

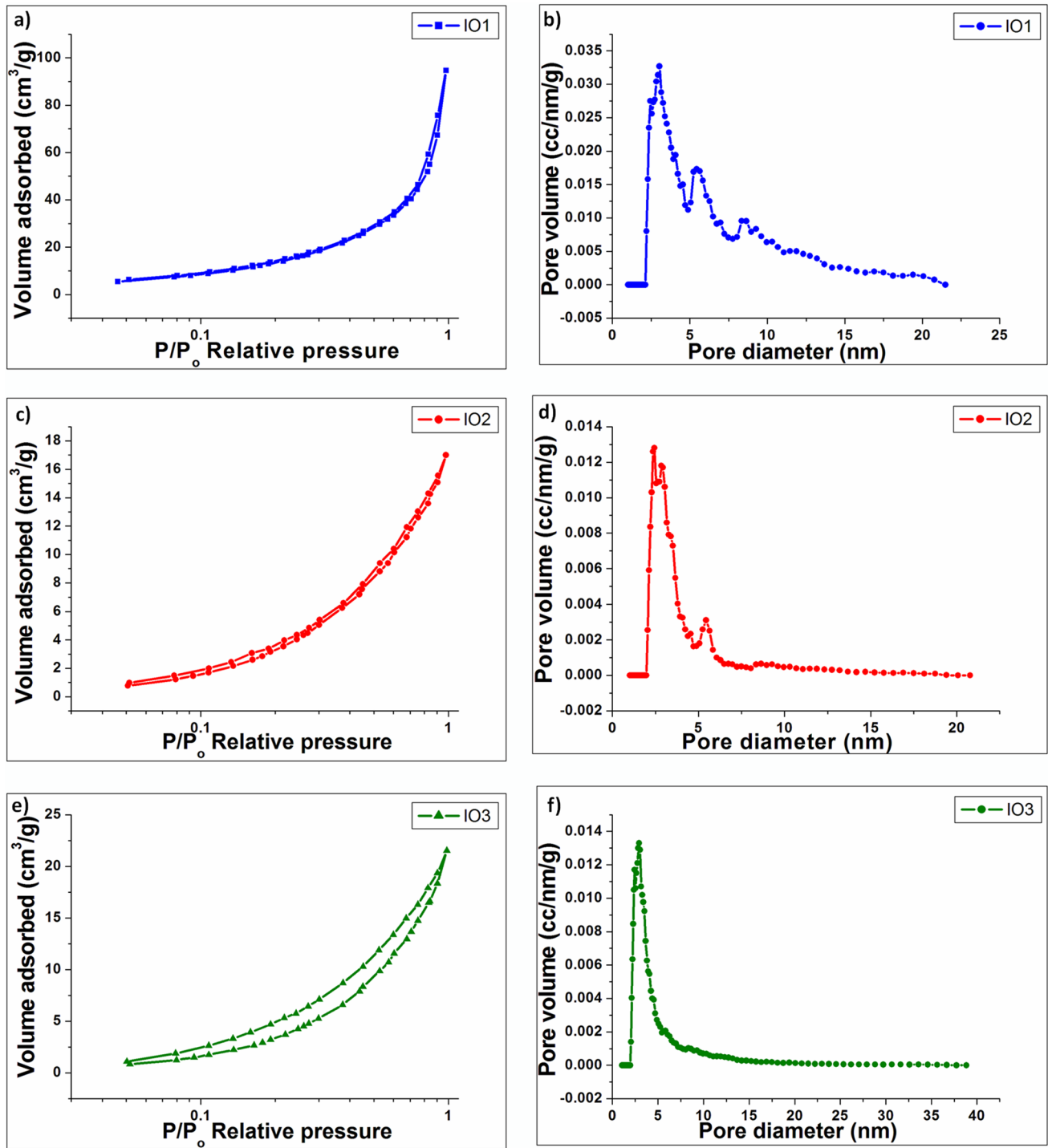


Fig. 5 N₂ adsorption–desorption isotherms and cumulative pore volume of the prepared iron oxides: (a, b) IO1, (c, d) IO2, and (e, f) IO3. Preference for color: online

significant decrease in body weights by 9.54 and 16.29%, respectively, while IO2 group demonstrated a significant increase in their body weight by 13.51%.

Effect of Three Formulations of IONPs on Liver Function

In order to find out which formulations of IONPs could cause hepatotoxicity and to evaluate the proper

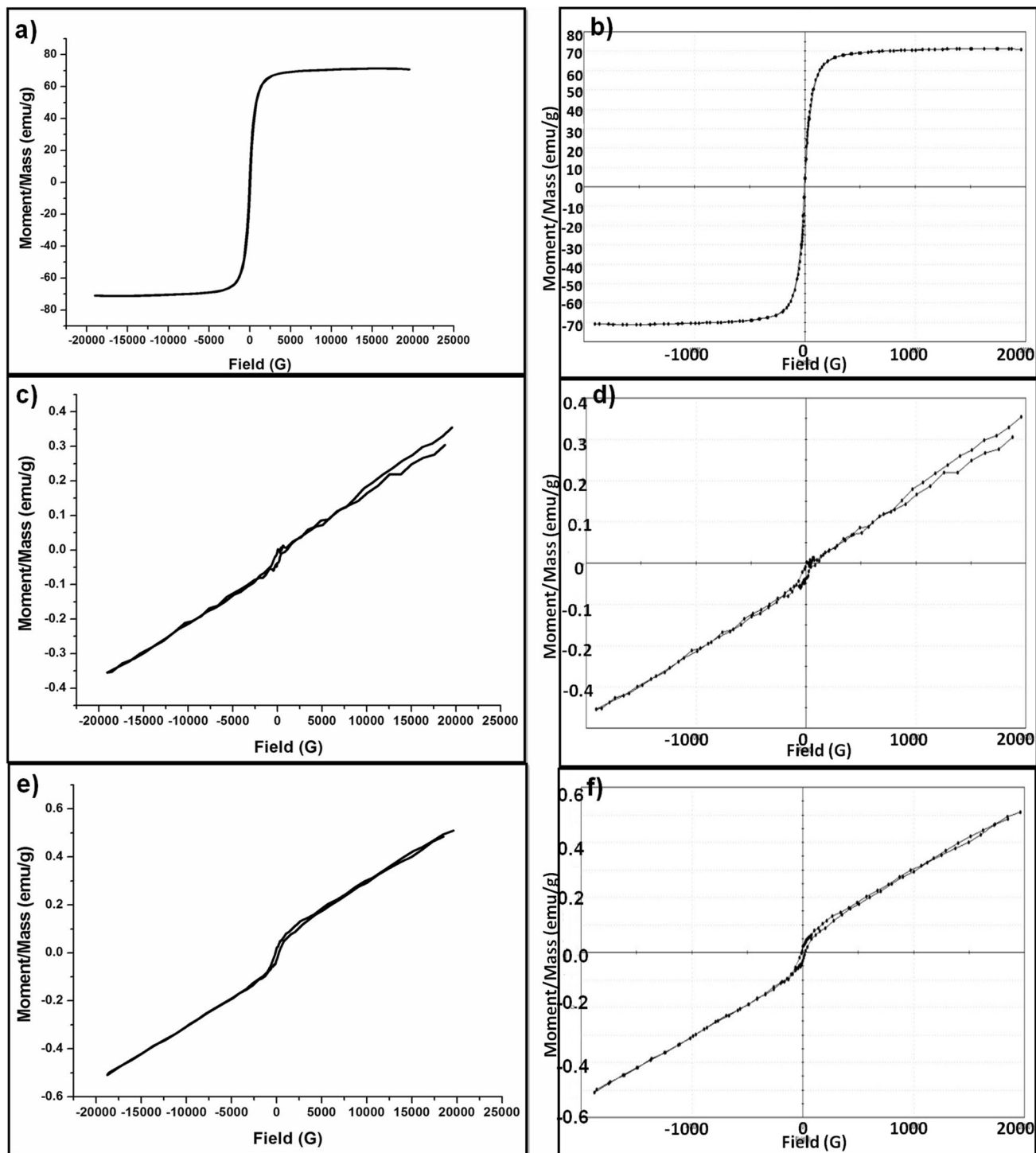


Fig. 6 Magnetic hysteresis enlarged partial (inset) curves of the prepared iron oxides: (a, b) IO1, (c, d) IO2, and (e, f) IO3. Preference for color: online

performance of the liver, serum levels of AST, ALT, and ALP were estimated. The administration of IO1, IO2, and IO3 resulted in a significant elevation in serum levels of AST by 13.80, 17.96, and 20.73% respectively, as

compared to negative control rats. However, IO2 exhibited an increase in ALT level by 30.22%, followed by 19.21 and 9.26%, respectively, for IO3, and IO1, as compared to negative control rats. On the other side, ALP demonstrated

Table 4 Magnetic parameters of IONPs obtained by different precursors

Sample	Magnetization (Ms) (G)	Coercivity (Hci) (emu/g)
IO1	71.273 ± 4.6	44.315 ± 2.70
IO2	0.35434 ± 0.05	9.7622 ± 0.30
IO3	0.50924 ± 0.02	171.12 ± 14.33

a significant elevation in IO3 by 35.5%, a mild increase by 8.35% in IO2, and a non-significant change in IONPs-Cl₃, as compared to negative control rats (Fig. 10).

Effect of IONPs on Oxidative Stress Markers

Oxidative stress in the liver and brain was analyzed by evaluation of MDA, GSH, and catalase. Determination of lipid peroxidation provides an estimate of the extent of oxidative injury on hepatic and brain cellular membranes. During evaluation of hepatic LPO, a statistically significant elevation in MDA was demonstrated in IO3 and IO2 by 44.5 and 34.05%, respectively, while IO1-exposed rats demonstrated an alteration by 14.43%, as compared to negative control rats. On the other side, hepatic GSH demonstrated a significant decrease by 58.61, 54.73, and 34.06%, respectively, for IO2, IO3, and IO1, as compared

Fig. 7 Particle size distribution curves of the prepared IONPs recorded by Zetasizer device. Preference for color: online

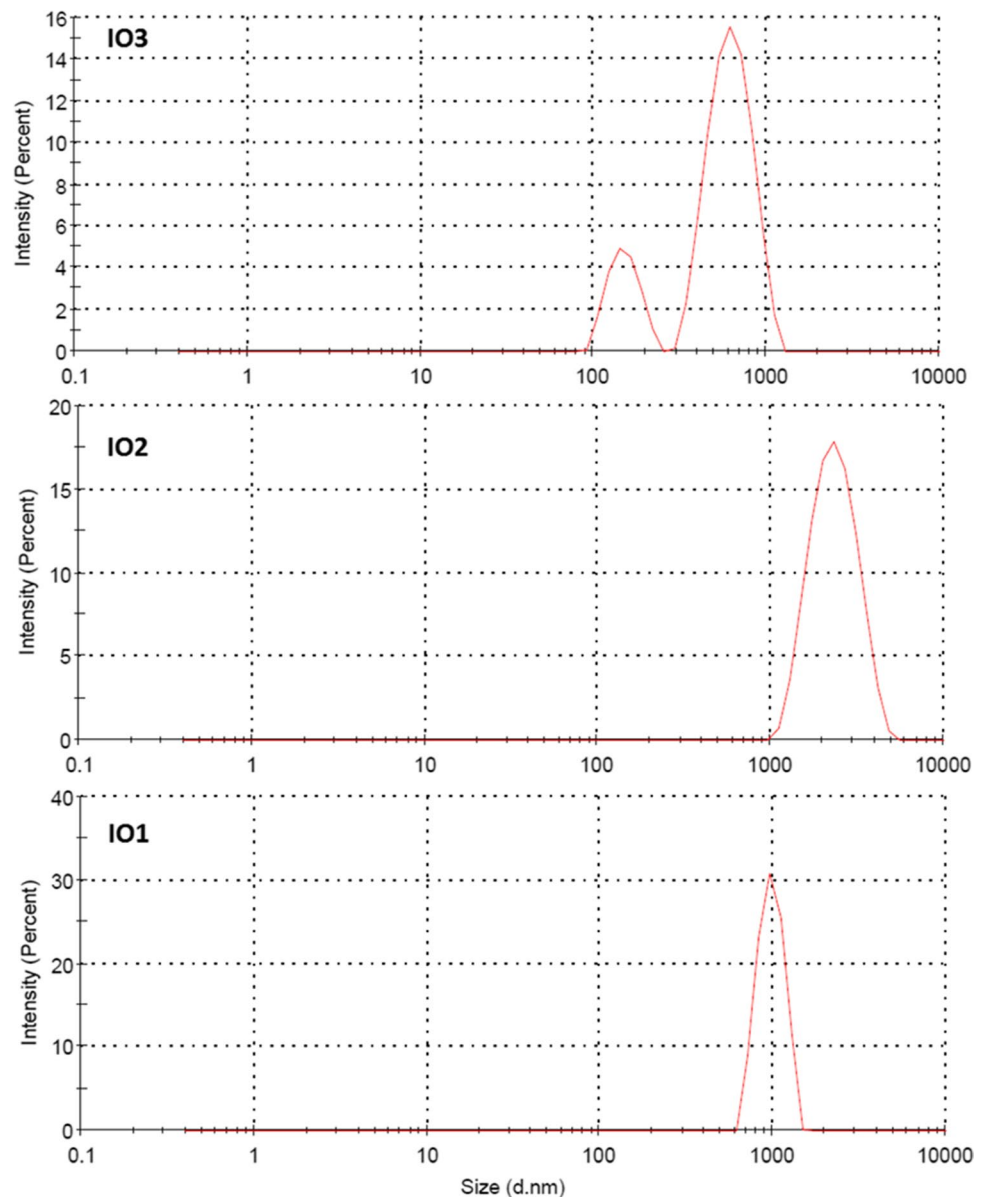
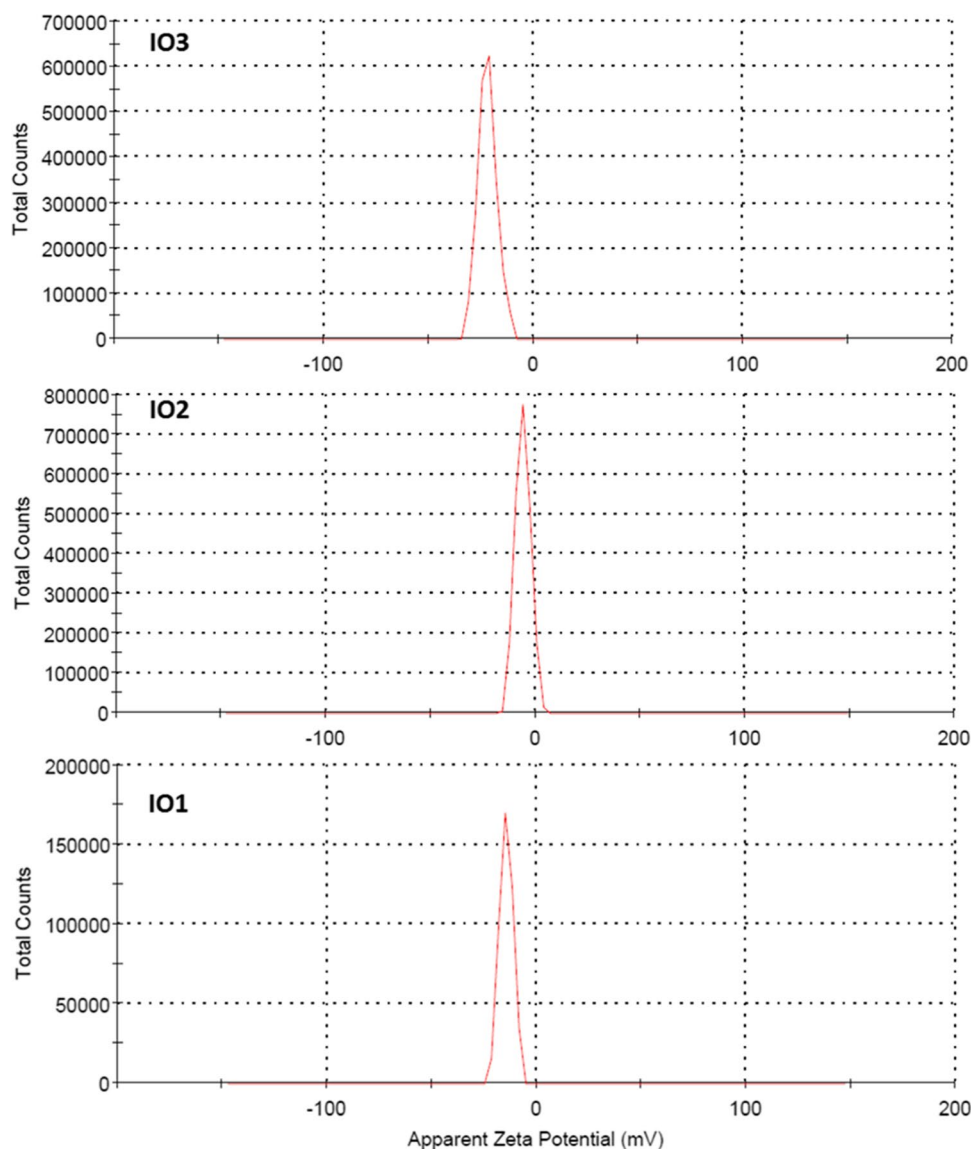


Fig. 8 Zeta potential profiles of the prepared IONPs recorded by Zetasizer device. *Preference for color: online*



to negative control rats. Considering hepatic CAT activity, IO1 (4.03%) showed a non-significant decrease, as compared to negative control rats. On the other hand, IO2 and IO3 showed a significant decrease by 38.92 and 22.15%, as compared to negative control rats (Fig. 11).

Regarding LPO activity in the brain, MDA showed a significant elevation in IO2, IO3, and IO1 by 34.42, 29.5, and 16.43%, respectively, as compared to negative control rats. Regarding brain GSH content, IO2, IO3, and IO1 demonstrated a significant decrease by 54.11, 40.68, and 30.09%, respectively, as compared to negative control rats. Similarly, brain CAT activity demonstrated a non-significant change for IO1-exposed rats, while IO2 and IO3 showed a significant decrease by 46.05 and 30.26%, respectively, as compared to negative control rats (Fig. 12).

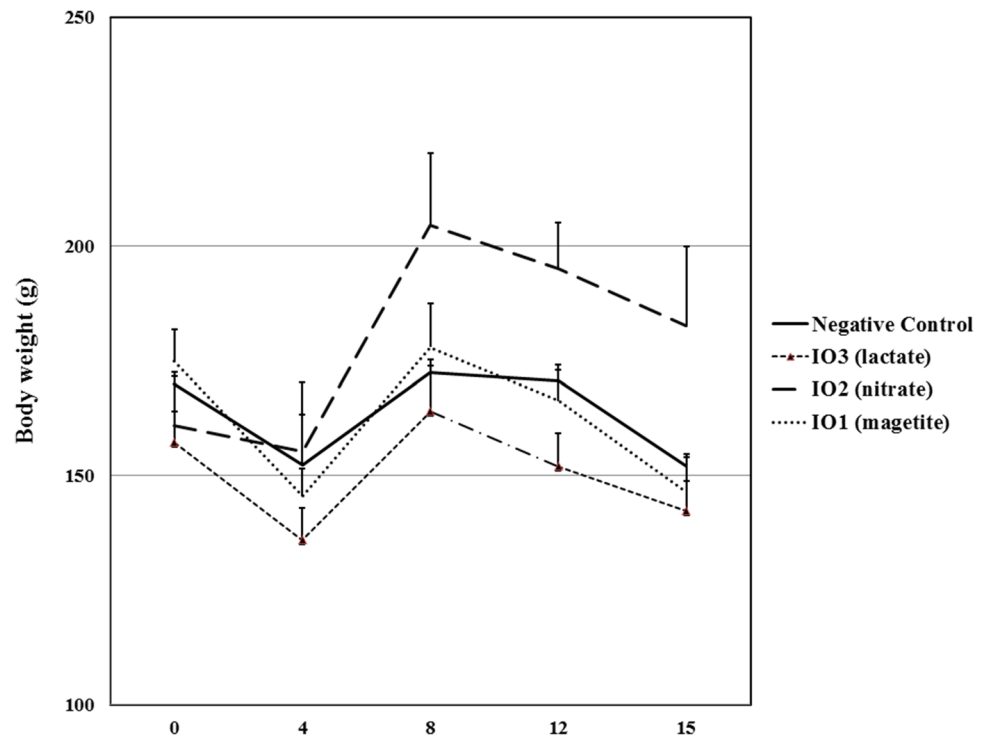
Iron Content in Hepatic and Brain Tissues

In order to analyze the uptake of IONPs in rats' liver and brain, 5 days after the last administration of IONPs, the total Fe content in the liver and brain was measured, relative to control using ICP-OES.

Regarding the total Fe content in the liver, IO3 (83.71%) > IO1 (27.64%) > IO2 (10.3%), as compared to Fe content in negative control rats. On the other hand, Fe content in the brain, IO2 (46.51%) > IO1 (40.4%) > IO3 (35.04%), as compared to Fe content in negative control brains.

The highest hepatic content of IO3 (83.71%) signifies the hepatic uptake of IO3 after oral administration and subsequent degradation into iron constituents, and partial deposition in the hepatocytes. On the other side, IO2 (46.51%) was highly up taken and deposited in IO2-exposed brains. The

Fig. 9 Body weights of Wistar rats following administration of different formulations of IONPs recorded twice a week for 15 days at time intervals of 0, 4, 8, 12, 15. Groups: Negative control rats and IONP-exposed rats: IO3 (lactate), IO2 (nitrate), IO1 (chloride). Results are expressed as mean values \pm standard error of the mean (SE) for $n=6$ rats per group, using one-way analysis of variance (ANOVA) followed by Tukey's test as the post hoc analysis



percent of change of IONP content in the liver and brain tissues is illustrated in Fig. 13.

Subcellular Localization and Ultrastructure Alteration in the Liver and Brain

After oral administration, IONPs circulate in the blood and reach the liver and brain. TEM findings confirmed alterations within the tissue ultrastructure coupled with IONP deposition. Ultrastructural investigation showed the subcellular localization of IONPs that could underlie the pathological changes and biochemical alteration in the liver and brain (Figs. 14 and 15).

The ultrastructural observation of the hepatocyte's nucleus had been performed by using TEM and the results are demonstrated in Fig. 14(A–D). As shown in Fig. 14(A), ultrathin sections of normal liver tissue showed hepatocytes with normal round nuclei, and a distinct nuclear membrane (NM). In addition, there was no breakage of organelles, including mitochondria and flattened intact and well-developed rough endoplasmic reticulum (RER); in addition, glycogen (G) granules were observed. The hepatocyte ultrastructure is clearly preserved in control livers.

Using TEM revealed the presence of swelling mitochondria (m) presence of condensed and scattered chromatin (Ch.) in the hepatocytes of IO3- and IO2- exposed rats. Nuclear membranes exhibited dense and irregular outline as compared to the nuclear membranes in control

hepatocytes alongside with nucleolus collapse. IONP accumulations were detected in different regions of the hepatocytes, as individual free NPs or as aggregates (Fig. 14(B, C)). IO3 clusters were observed in the nucleus and cytoplasm of hepatocytes in the form of agglomerates (Fig. 14(B)). IONPs were seen clustered together throughout the cytoplasm in the hepatocytes (Fig. 14(B, C)). In addition, TEM observation revealed that IONP aggregates were uptaken by lysosomes that appeared as dark and vacuolated organelles. IO3- and IO2-exposed rats displayed cytoplasmic alterations in hepatocytes, such as mild vacuolization and swollen fat globules (f) of various sizes. On the other side, IO1-exposed hepatocytes (Fig. 14(D)) demonstrated the least subcellular localization of NPs and consequently the least ultrastructural modifications in the hepatocytes.

The ultrastructure of brain cells (neuropils) in the control group rats showed normal appearance (Fig. 15(A)). The ultrastructural photomicrographs of brain cells presented in Fig. 15(B–D) clearly show the ultrastructural effects of NPs. Differently, selected structural alterations evidenced in the brains of both IO2- and IO3- exposed rats were presented. TEM images of IO3-exposed brains demonstrate ultrastructural alterations in neuronal mitochondria (m), which were swollen with fragmentation of the cristae (cristolysis), in addition to nuclear degeneration (Fig. 15(B)). IO2-exposed brain cells (Fig. 15(C)) were featured by the presence of elongated

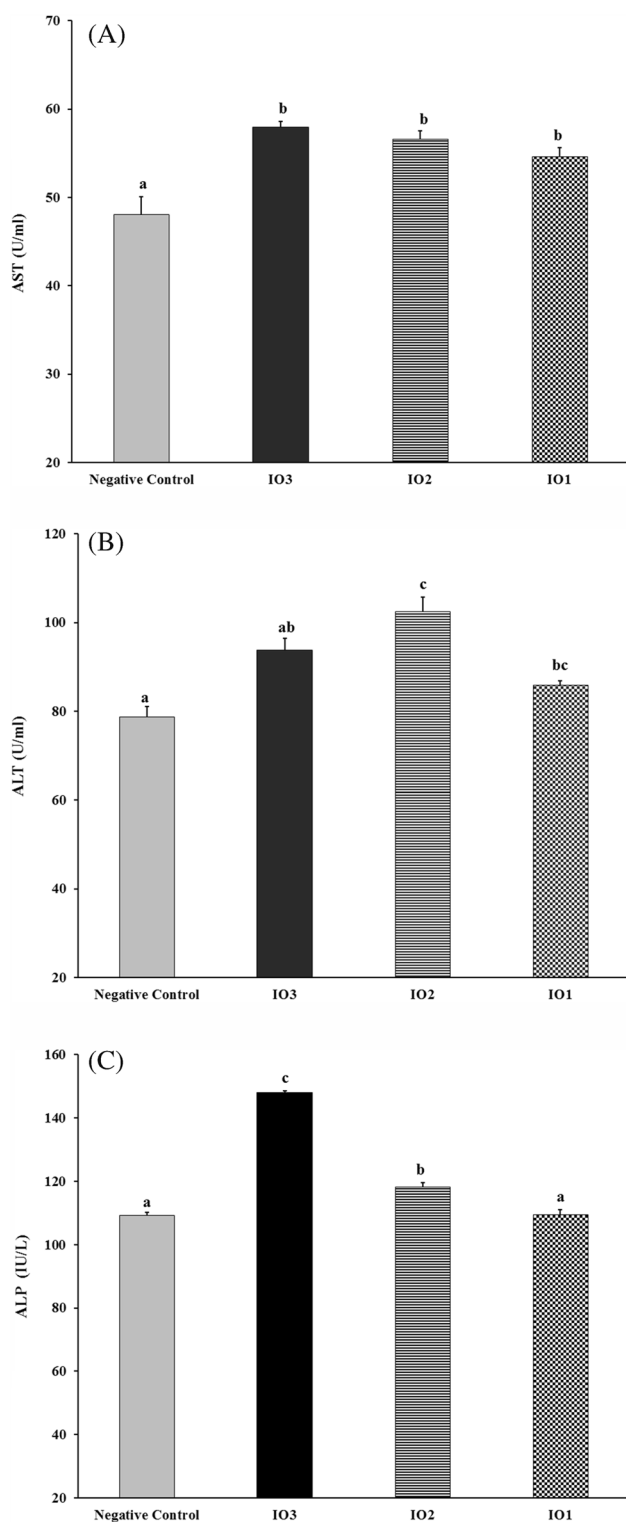


Fig. 10 Effect of the three formulations of IONPs on liver function. Groups: Negative control rats and IONP-exposed rats: IO3 (lactate), IO2 (nitrate), IO1 (chloride). Results are expressed as mean values \pm standard error of the mean (SE) for $n=6$ rats per group, using one-way analysis of variance (ANOVA) followed by Tukey's test as the post hoc analysis. Mean with different superscripts (a–c) are significant at $p \leq 0.05$. (A), (B), (C) Aspartate aminotransferase (AST), alanine aminotransferase (ALT), and alkaline phosphatase (ALP), respectively. Preference for color: online

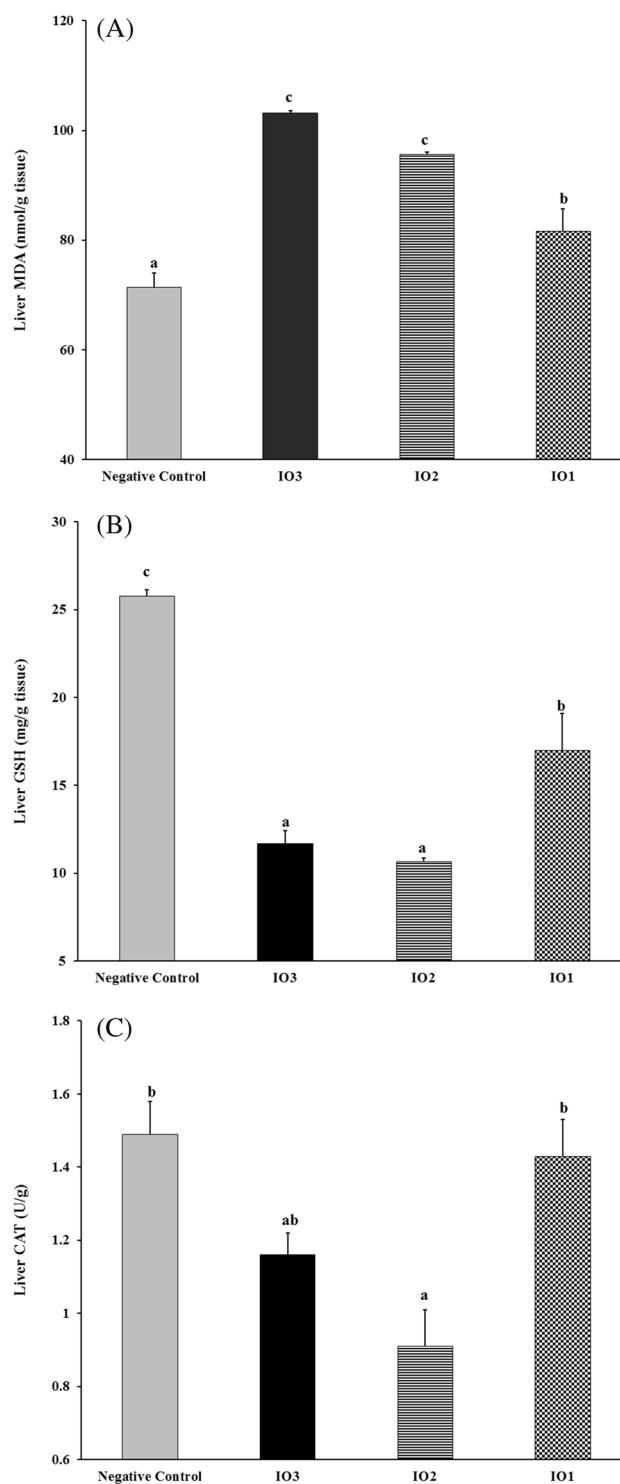


Fig. 11 Effect of the three formulations of IONPs on oxidative stress markers in the liver. Groups: Negative control rats and IONP-exposed rats: IO3 (lactate), IO2 (nitrate), IO1 (chloride). Results are expressed as mean values \pm standard error of the mean (SE) for $n=6$ rats per group, using one-way analysis of variance (ANOVA) followed by Tukey's test as the post hoc analysis. Mean with different superscripts (a–c) are significant at $p \leq 0.05$. (A), (B), (C) Malondialdehyde (MDA), reduced glutathione (GSH), and catalase (CAT), respectively. Preference for color: online

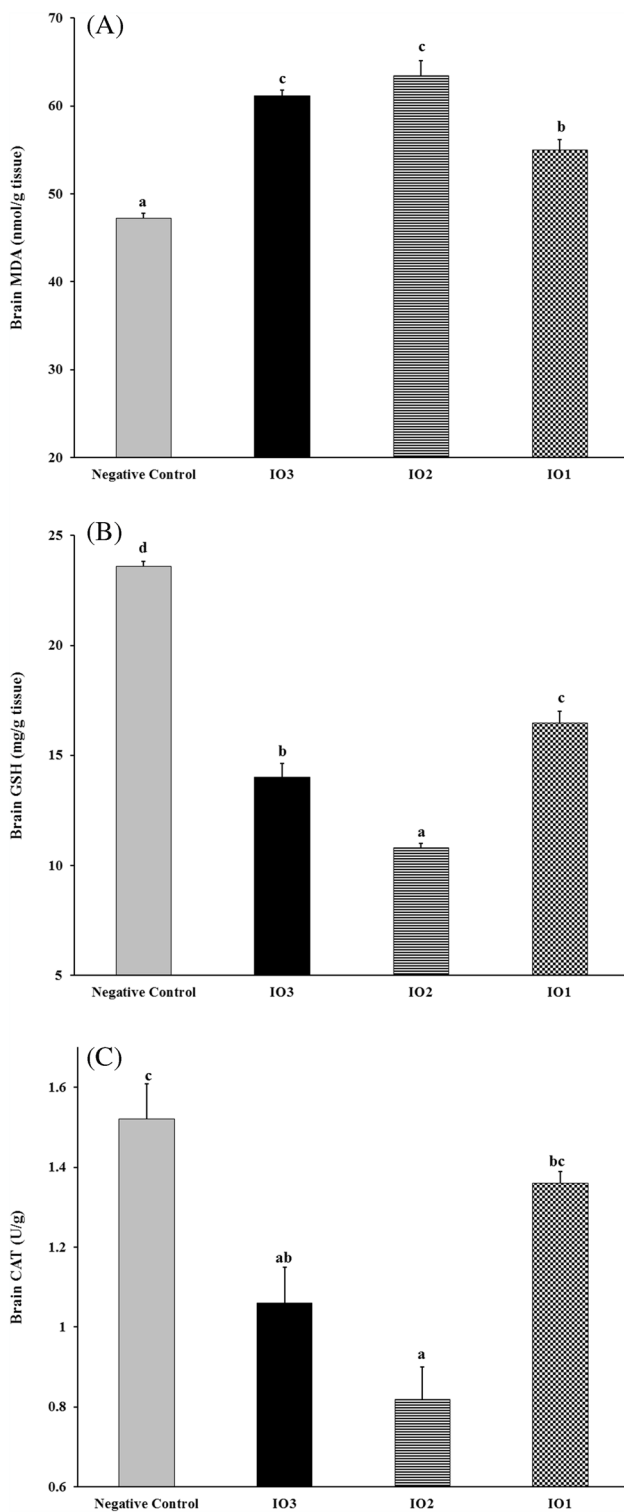


Fig. 12 Effect of the three formulations of IONPs on oxidative stress markers in the brain. Groups: Negative control rats and IONP-exposed rats: IO3 (lactate), IO2 (nitrate), IO1 (chloride). Results are expressed as mean values \pm standard error of the mean (SE) for $n=6$ rats per group, using one-way analysis of variance (ANOVA) followed by Tukey's test as the post hoc analysis. Mean with different superscripts (a–c) are significant at $p \leq 0.05$. (A), (B), (C) Malondialdehyde (MDA), reduced glutathione (GSH), and catalase (CAT), respectively. *Preference for color: online*

mitochondria (m). On the other hand, IO1-exposed brains (Fig. 15(D)) showed the least subcellular localization of IONPs and consequently the least ultrastructural alterations in the neural cells.

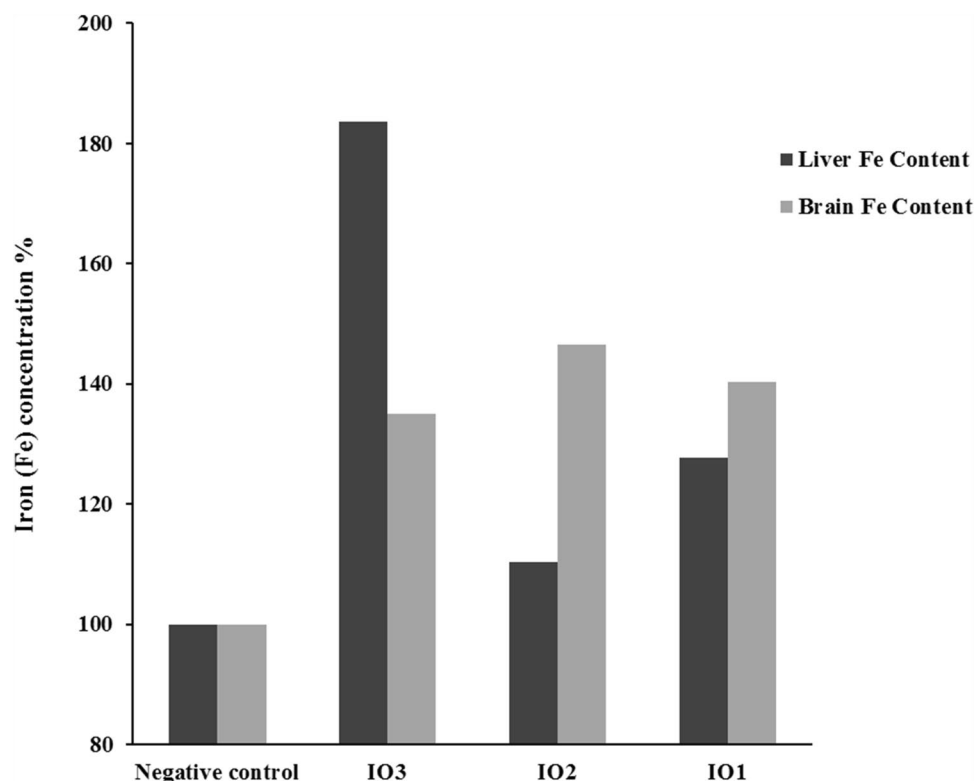
Discussion

The physical nature of the obtained IONPs in this study was evaluated by XRD techniques, where crystalline phase of magnetite was confirmed to IO1 sample and amorphous phases of Fe_2O_3 were detected to the other two samples (IO2 and IO3). This may be attributed to the applied annealed temperature at 200 °C according to previous literature [85–87]. This was also confirmed by the TEM results as IO1 sample exhibited semi-hexagonal nano-crystalline particles and the IO2 sample demonstrated amorphous nanospheres that include porous structure within the particle boundary, while sample IO3 demonstrated compact nanospheres like particles with no sign of porous structure. The precursor, as well as the synthesizing method, showed remarkable influence on the physical structure and morphological features of the achieved IONPs as affirmed by XRD and TEM results. On the other side, the chemical integrities of the fabricated IONPs were not alerted by the variation in the starting materials as confirmed by FTIR results.

Moreover, the BET surface area measurements revealed that the average pore diameter and pore volume were slightly changed with changing the starting material of the IONPs along with the appearance of their isotherms. In general, they exhibited type II hysteresis loop containing nano-pores (samples IO1 and IO2) and nanoparticles free pores (sample IO3). This difference could be owed to the influence of different precursors and the different synthesizing conditions. Previously, similar variations in the BET surface area parameters were noticed for mesoporous silica fabricated with different methods including hydrothermal synthesis [88]. It was noticed also that magnetization features of the obtained IONPs demonstrated huge values' variations, which suggested the great impact of starting materials on the magnetic properties on the final produced nanoparticles.

The particle size distribution and the charges allocated on their surfaces play a significant role on the mechanism of nanoparticles-cells interactions. Therefore, defining these important factors is very valuable while considering nano-carriers. For the IONPs, a negative zeta potential can be an advantageous property for better cell internalization. The low zeta potential distribution values for all of the samples studied suggested that the particle suspensions are on the verge of being unstable. Magnetic nano-carriers demonstrated impressive adjusted drug delivery in our previous research [89].

Fig. 13 Percentage change of the uptake of IONPs and the iron (Fe) content in liver and brain tissues, as compared to negative control rats. IONP-exposed groups: IO3 (lactate), IO2 (nitrate), IO1 (chloride)



In vivo experiments were performed using three differently formulated IONPs, regarding that IONPs are non-stable metallic NPs that display relative high rates of ion release. Female rats are utilized as they are slightly more sensitive according to OECD guidelines [64]; moreover, it was observed that NPs tend to accumulate in female reproductive organs and present a potential threat to the susceptible female population [90]. Adult female Wistar rats were exposed orally to three formulations of IONPs (IO1, IO2, and IO3) to evaluate their toxic potential.

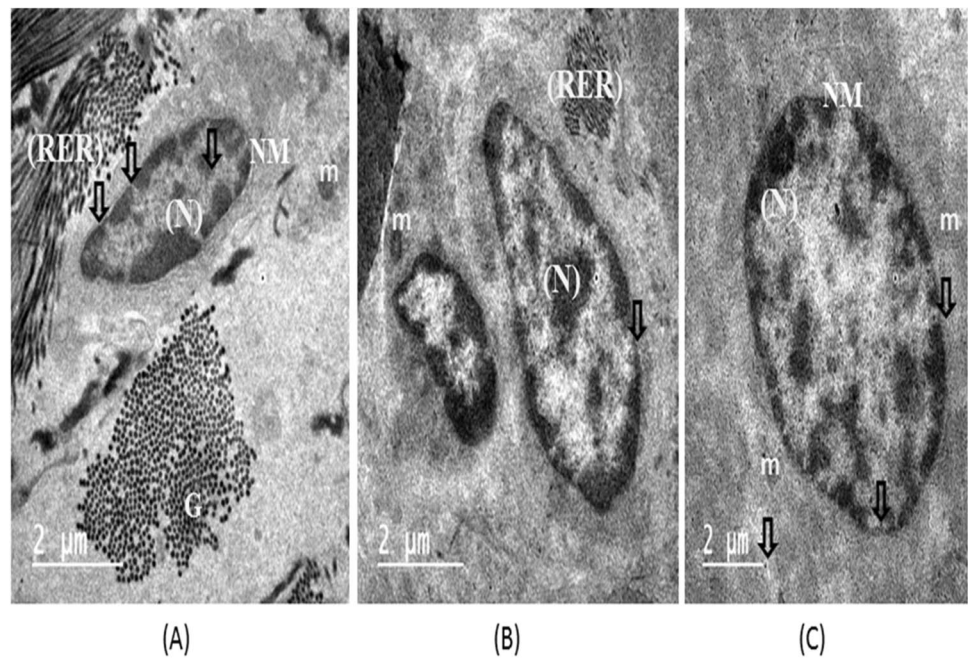
No mortality was observed in the animals in any IONP-exposed groups. Treatment with a dose of 100 mg/kg body weight of three different formulations of IONPs resulted in variations in clinical signs. IO1-exposed rats demonstrated no clinical signs or symptoms of toxicity or mortality; these rats exhibited normal appearance and non-neurotoxic behavior. IO1-exposed rats showed the safest toxicological profile regarding appearance and behavior, in comparison with IO2 and IO3. The order of clinical signs based toxicity is IO2 > IO3 > IO1. Published data regarding toxicity of IONPs are not consistent, which might be due to variation in IONP physicochemical characteristics (*e.g.*, size, shape, and surface charge) and experimental conditions (*e.g.*, animal models, administration route, and quantification techniques) used in different studies [91, 92]. These physicochemical characteristics are strongly correlated with the interactions with biological macromolecules (*e.g.*, lipids), cellular uptake, in vivo fate, and toxicity of IONPs [92].

Estimation of body weight was considered a principal toxicity index for rats; however, a previous toxicological study demonstrated that relative organ weights terms (organ to body weight ratio) could increase the error rate and lead to mis-interpretation of toxic potential [93]. Changes in body weight could be linked to toxicity of administered chemical or toxicant [24]. Herein, the IONPs administration resulted in significant alterations in body weights of rats in comparison to the control; this could represent a part of the symptoms of toxic events associated with IONPs exposure. Herein, IO2 (nitrate-IONPs)-exposed rats demonstrated the highest body weight, as compared to their initial body weight; this could be justified by the increased accumulation of fluids in the abdominal area; a clear toxicity sign.

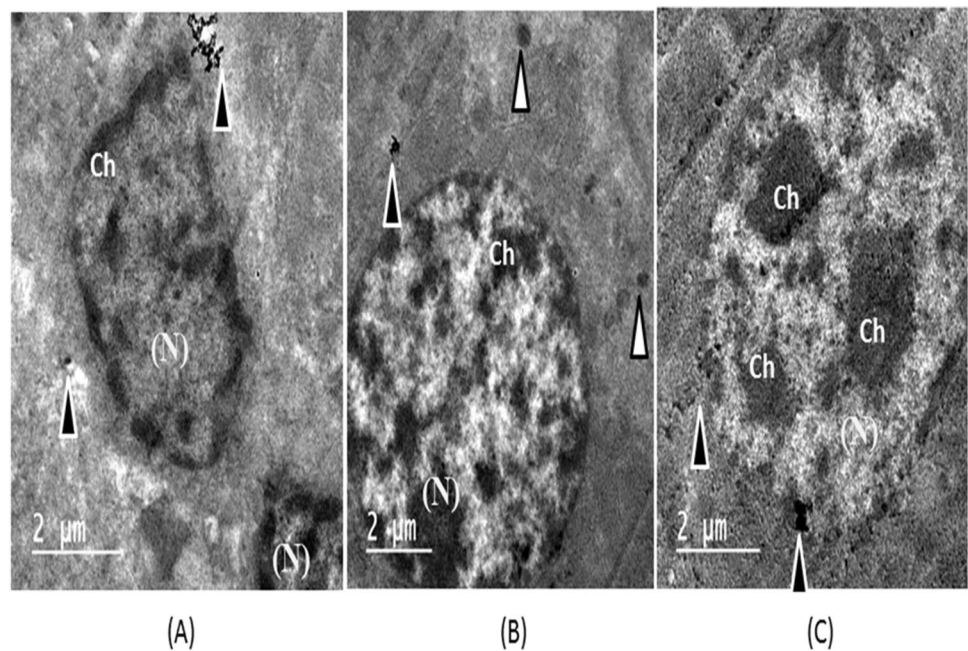
Several studies revealed that the distribution or deposition of NPs in the organs might lead to the organ toxicity; the liver and brain are among the major target organs of nanotoxicity [27, 94, 95]. Therefore, for nanotherapeutic application, it is vital to avoid opsonization to keep NPs in circulation for longer period and increasing the opportunity for targeted delivery [96]. The liver is the main organ of the mononuclear phagocytic system (MPS) that is exposed to systemically administered NPs and where NPs are likely to end up [97, 98]. Regarding liver function, ALT and AST are two of the most reliable markers of hepatocellular injury. The administration of IONPs resulted in significant elevations in serum levels of AST and ALT in the following order IO2 > IO3 > IO1. The elevation of the activities of AST and

Fig. 14 TEM ultrastructure images from liver tissue of control (A) and IONP-exposed rats (B–D). Rats were administered IONPs through gavage for 14 days and sacrificed 5 days after the end of the treatment.

A: Ultrastructure of Control liver: the hepatocytes have normal ultrastructural features, demonstrating normal nucleus (N) with regular nuclear membrane (NM), containing nucleopores (empty arrows), mitochondria (m), well-developed rough endoplasmic reticulum (RER), and glycogen granules (G). **B: Ultrastructure of IO3-exposed liver:** dense smaller isolated clusters “aggregates” were recognized free in cytoplasm (black arrowheads) and presence of condensed chromatin (Ch.). **C: Ultrastructure of IO2-exposed liver:** dense nano-clusters were observed in lysosomes (white arrowheads) and some smaller isolated aggregates were identified free in cytoplasm (black arrowheads). Nanoaggregates were mainly deposited in lysosomes (white arrowheads), in addition to the presence of elongated mitochondria (m) and condensed chromatin (Ch.). Notice the presence of cytoplasmic vacuolization with containing numerous fat globules (f). **D: Ultrastructure of IO1-exposed liver:** showed almost normal appearance with normal structure of hepatocytes. Preference for color: online



A: Ultrastructure of Control liver

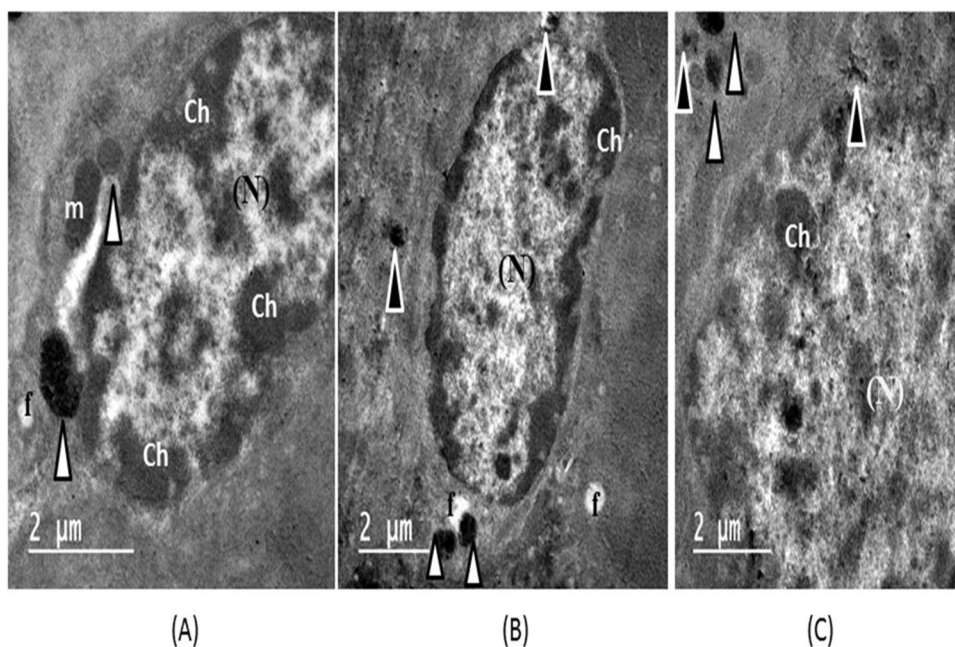


B: Ultrastructure of IO3-exposed liver

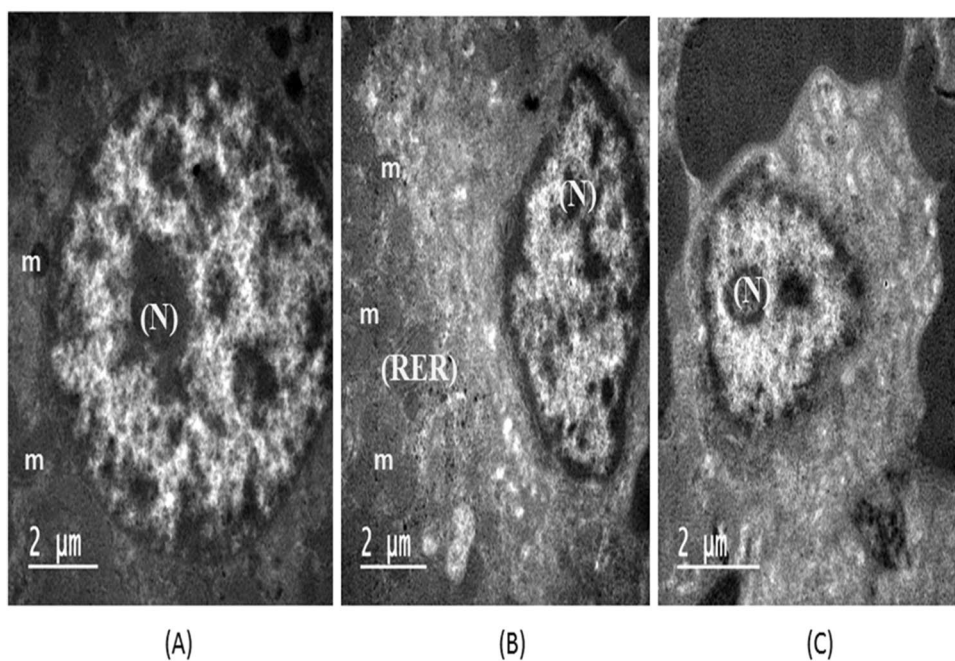
ALT might be linked to hepatotoxicity [24, 99, 100], due to the uptake and deposition of NPs by the MPS hepatocytes and Kupffer cells [101]. ALT is considered more specific than AST as it is a cytosolic enzyme mainly located in the hepatocytes, while AST exhibits cytosolic and mitochondrial forms and exists in different tissues [101]. Therefore, the significant elevation of ALT confirms hepatotoxicity [102].

IONP-induced hepatotoxicity occurs as damaged hepatocytes release this cellular enzyme into blood stream. The translocation of NPs into the blood stream facilitates their interaction with opsonin proteins that subsequently enable resident macrophages of the MPS to easily recognize and engulf these NPs, thereby resulting in uptake and deposition of NPs in MPS organs, such as the liver and spleen [103]. In

Fig. 14 (continued)



C: Ultrastructure of IO2-exposed liver



D: Ultrastructure of IO1-exposed liver

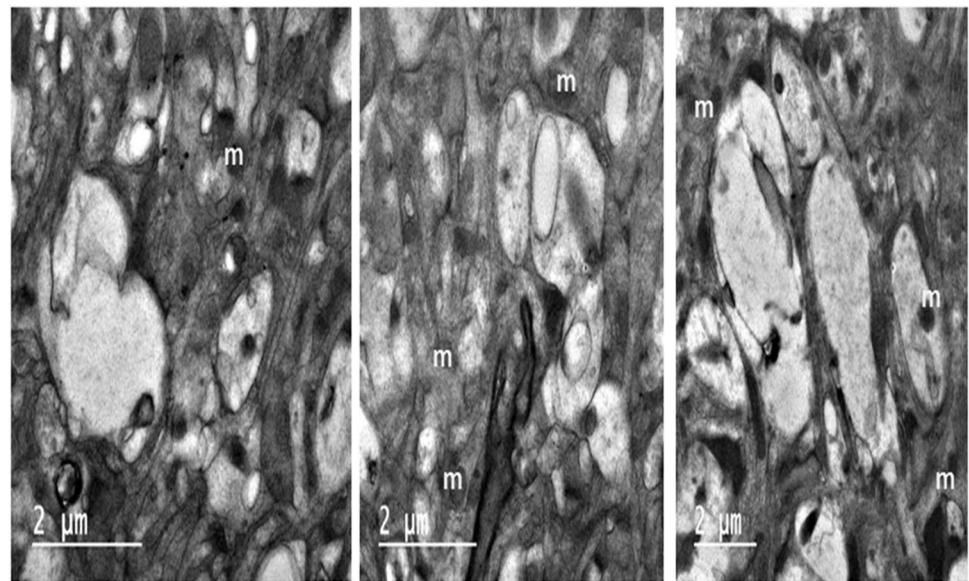
addition, after cellular distribution of IONPs, iron dissolved from the NP core and is reduced to ferrous iron (Fe^{+2}) under acidic conditions [104]. During excess iron exposure, the liver tends to protect other tissues from iron-induced cellular toxicity through increasing iron storage, which might result in ROS-induced hepatic damage [105]. Using TEM, the presence of IONPs in hepatocyte can provide direct evidence of IONP-induced hepatotoxicity and refers to the

obvious biochemical alterations in hepatocytes at the subcellular and cellular levels.

The hepatic accumulation and deposition of IONPs resulted in disturbance of the liver function indices, which are markers indicating oxidative stress-induced hepatic injury. In this study, IO3 and IO2 induced hepatic damage, as confirmed by the increased serum ALT and AST activities and TEM analysis. This elevation in liver enzymes runs in

Fig. 15 TEM ultrastructure images from brain tissue of control (A) and IONP-exposed rats (B–D). Rats were administered IONPs through gavage for 14 days and sacrificed 5 days after the end of the treatment.

A: Ultrastructure of Control brain: showed normal structure of the neuronal cell with normal appearance of mitochondria (m) and well-defined neural structure. **B: Ultrastructure of IO3-exposed brain:** Nano-aggregation of IONPs inside the neuronal cells (black arrows); NPs are observed as dark nanosized granules. In addition, a mitochondrial aberration (cristolysis) could be visualized that appeared as dark circular objects (m). It was also demonstrated the shrunken and degenerated neuronal cells and the condensed chromatin in the nucleus (N). The presence of myelinated (thick black arrow) and demyelinated (thick white arrow) nerve fibers could be observed, in addition to degeneration of nerve fibers (black triangle). **C: Ultrastructure of IO2-exposed brain:** abnormal structure of the neuronal cell with deformed appearance of elongated mitochondria (m). The presence of myelinated (thick black arrow) and demyelinated (thick white arrow) nerve fibers could be observed, in addition to degeneration of nerve fibers (black triangle). **D: Ultrastructure of IO1-exposed brain:** showed almost normal appearance with normal neuronal structure. *Preference for color: online*

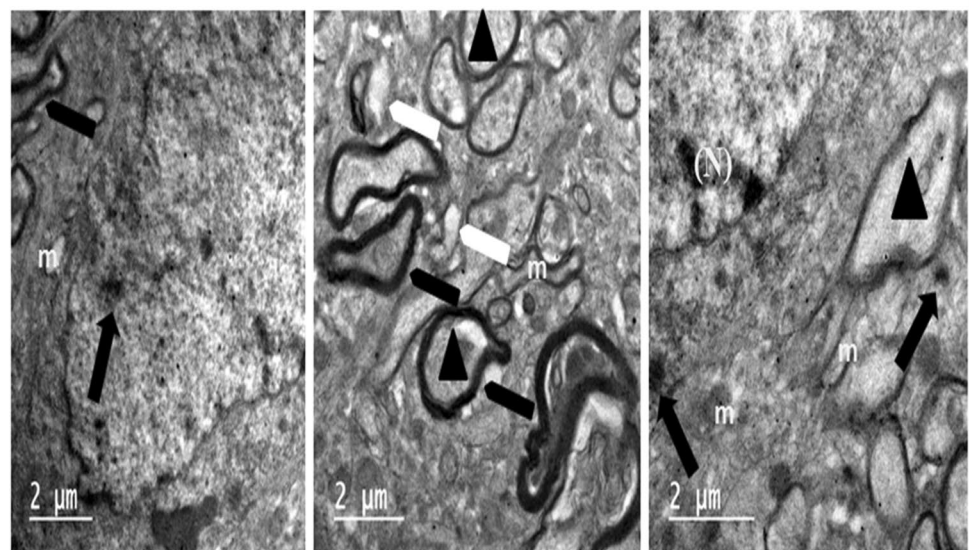


(A)

(B)

(C)

A: Ultrastructure of control brain cell (neuropil)



(A)

(B)

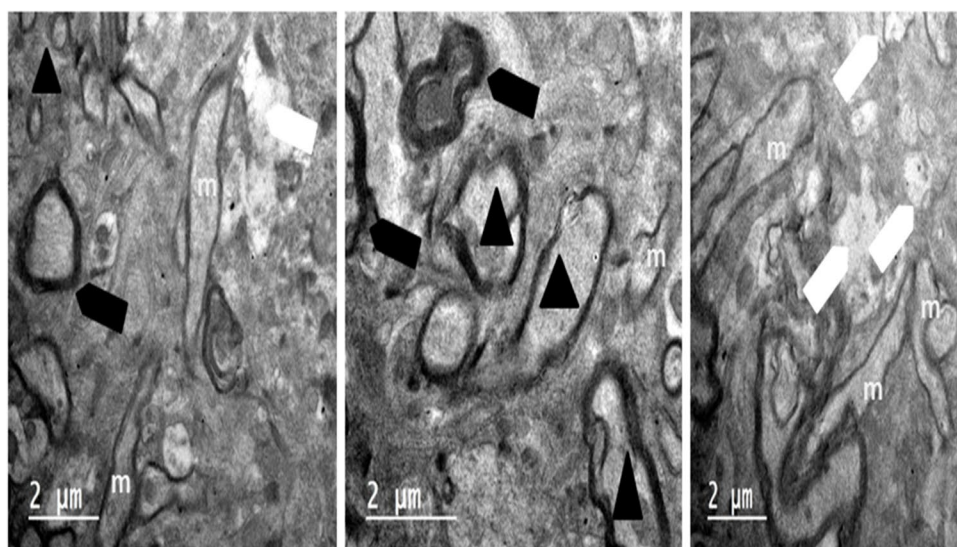
(C)

B: Ultrastructure of IO3-exposed brain cell (neuropil)

agreement with a study by Shirband et al. [106] that showed destruction of liver cells and obstruction of bile ducts. These observations could be considered substantiation for acute hepatotoxicity in rats. In addition, ALP demonstrated significant elevation in rats exposed to IO3 and IO2 by 1.36 and 1.084 folds, respectively, while rats exposed to magnetic IO1 showed normal values with respect to the control group. ALP is present in several tissues, including the liver, bone, kidney, and white blood cells, and is measured to detect the

liver disease or bone disorders [107]. Thereby, the release of ALP into the blood stream reflects damage to these organs. The results indicate a safe toxicological profile regarding the therapeutic use of IO1. Besides hepatotoxicity (liver dysfunction), IONP accumulation might induce generation of reactive oxygen species (ROS) and cause oxidative stress resulting in the lipid peroxidation, inhibition of antioxidant enzymes, depletion of glutathione, and endoplasmic reticulum stress [94, 108]. Orally administered IONPs reach the

Fig. 15 (continued)

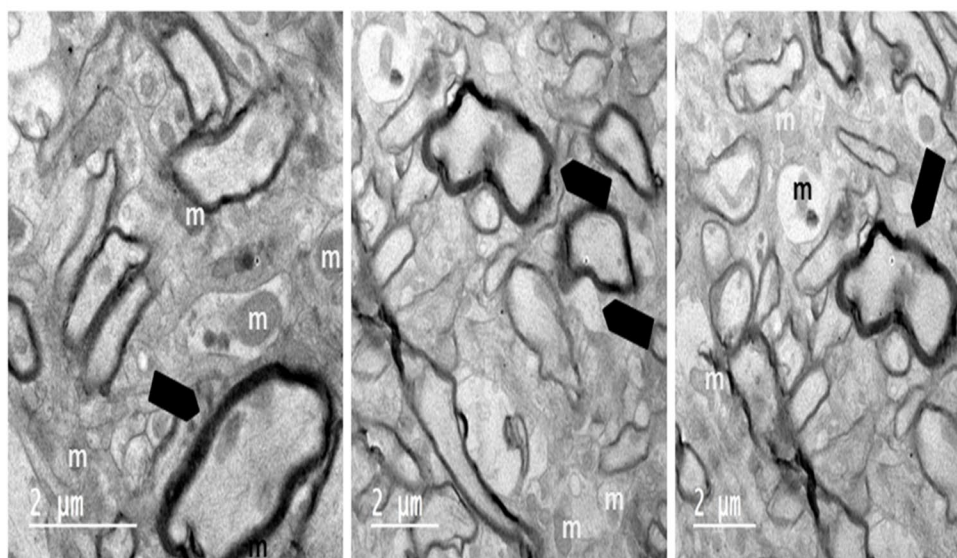


(A)

(B)

(C)

C: Ultrastructure of IO2-exposed brain cell (neuropil)



(A)

(B)

(C)

D: Ultrastructure of IO1-exposed brain cell (neuropil)

liver, *via* the blood stream, and induce local oxidative reactions. The effect of IONPs on hepatic function stimulated the antioxidative stress response [108]. Herein, administration of IO3 and IO2 significantly increased MDA and depleted GSH. These findings were in accordance with those of Reddy et al. [94] and Askri et al. [108]. Decline in GSH content might be linked to increase scavenging of hepatotoxicity-induced ROS production. CAT catalyzes hydrogen peroxidation reaction and is generally responsible for removing generated hydrogen peroxide (H_2O_2) [105]. + Suppression

of hepatic CAT activity might be attributed to the IONP-increased generation of free radicals.

Taken together, significant alterations in lipid peroxidation, as well as AST, ALT, and ALP serum levels in IONP-exposed rats, confirm that IO3 and IO2 could result in loss of the functional integrity of the cell membranes and cause the leakage of these liver enzymes [105, 109], indicating hepatocellular injury. In contrast, the lack of significant alterations in lipid peroxidation as well as liver enzymes in IO1-exposed rats confirms that this formulation did not affect

the functional hepatocellular integrity. This signifies the safe and good biocompatibility with only slightly elevated ALP, ALT, and AST levels unaccompanied by any obvious ultrastructural changes. A dose of 100 mg/kg body weight of IO1 was capable of retaining hepatic functional integrity, even though with some enhancement of “redox defenses.” IO1-chloride induced only minimal levels of oxidative stress and therefore IO1 could be used for nanotherapeutics.

As recommended by a previous study by Easo and Mohanan [105], we aimed to evaluate the oxidative stress hepatotoxicity and neurotoxicity of repeated administrations (14 days) of IONPs to explore the potential of utilizing these NPs for biomedical application. Similarly, IONP-induced oxidative stress in the brain was determined by assessing GSH and MDA levels, in addition to CAT activity. As demonstrated, exposure of rats to IO2 and IO3 significantly increased lipid peroxidation, as well as induced significant reduction in GSH content and CAT activities in comparison to control group.

Iron is an essential factor for proper function of CNS; it is involved in synthesis and metabolism of neurotransmitters, myelin production, oxygen transportation, and oxidative phosphorylation [110, 111]. Furthermore, oligodendrocytes, which are responsible for myelin production, have the highest Fe content in the brain [112]. However, there is a strong connection between Fe overload or accumulation in the brain and Fe-induced neurotoxicity [111]. The brain is more vulnerable to oxidative stress due to the reduced levels and activities of antioxidant enzymes including CAT, high lipid content, and oxygen turnover and low mitotic rate [113]. Therefore, abnormal iron homeostasis within the brain is capable of generating ROS-induced neurotoxicity and disrupting the function of BBB [114]. During exposure to IONPs, rate of lipid peroxidation surpasses antioxidant capability in the brain [115]. IONPs affect several neural pathways involved in brain activity and function, indicating their neurotoxic potential [108]. The high surface area of deposited NPs may contribute to cellular interaction and ROS generation; these reactions cause neural damage and increased risk of developing neurodegenerative disorders [116]. Therefore, it is necessary to study the potential of IONPs to cause oxidative stress in the brain.

Similarly, IONP exposure was capable of inducing oxidative stress in the brain. Oxidative stress is the main mechanism of Fe-induced toxicity, and this could be attributed to the “flexible nature and redox potential” of Fe, as a transition metal, that is able to give and receive an electron; thus, excessive content of iron can be cytotoxic and neurotoxic [110, 117]. Consequently, the oxidation state of iron (Fe^{2+} or Fe^{3+}) in NPs is an important factor to estimate NP toxicity, for example, Fe^{3+} in Fe_2O_3 is more genotoxic than Fe^{2+} in Fe_3O_4 [118], which is in the same line of our findings.

Oxidative stress is one of several mechanisms leading to nanotoxicity [119], as the biological enzymatic activity attacks NPs and releases iron ions, resulting in ROS production, damage of macromolecules, and finally leading to cellular death [120]. Naturally, redox-active iron ions (Fe^{2+}) participate in ROS-generating reactions (*e.g.*, Fenton reactions) through reacting with H_2O_2 and produce OH^\bullet radical [121]. “ H_2O_2 -induced apoptosis” is another mechanism that increases intracellular iron pool, where iron-induced oxidative stress is capable of damaging lysosomes, in addition to disrupting iron hemostasis through increasing transcription of ferritin and loss of transferrin receptor on the surface of cellular membrane [122]. Ferritin binds to excess iron in the cytoplasm, and the free iron could elaborate toxic potential; the intracellular amount of Fe^{2+} , in presence of both oxygen and GSH, is also able to produce ROS [123] that might react with cellular membranes resulting in lipid peroxidation and the production of toxic MDA [114]. Moreover, this might result in mitochondrial dysfunction through disrupting mitochondrial permeability transition pore that results in the release of Ca^{2+} and cytochrome C into the cytoplasm, causes disruption of ATP synthesis and Ca^{2+} buffering, and finally activates apoptosis [124]. Mitochondrial dysfunction was obvious in ultrastructural investigation.

Bioaccumulation and retention of IONPs in the liver and the brain triggered the oxidative stress and affected the cellular ultrastructure. Cellular deposition of iron depends on several factors including the initial concentration, size, shape, and a functional group, in addition to cell type [125]. Deposition of iron ions is capable of inducing cellular apoptosis known as “ferroptosis” through stimulating morphological, biochemical, and genetic features distinct from apoptosis, necrosis, and autophagy, such as smaller mitochondria, elevated cytotoxic lipid ROS, decreased dopamine, and increased membrane density [115].

IONP-induced oxidative stress was evidenced by elevation of MDA and depletion of GSH and CAT in the liver and the brain. Exposure of rats to IO2 and IO3 induced oxidative stress that might be co-related with hepatic dysfunction and brain injury. To counteract IONP-induced oxidative stress, cells utilize antioxidant enzymes such as GSH and CAT to remove the redundant ROS and to attack IONPs that results in release of iron ions and subsequently increased iron pool, contributing to oxidative stress. The variation in the ability of IONP formulations to generate oxidative stress might be related to the physicochemical properties of NPs [115]. This variation in the cytotoxicity of the three different IONPs might be size dependent, as small NPs degrade sooner than the large NPs, which tend to agglomerate; then, they are easily sequestered by macrophages [126]. In addition, smaller NPs present more reactive surface areas therefore generate more ROS, as compared with the larger particles [118]; for instance,

10 nm NPs may induce oxidative stress in endothelial cells [127]. In contrast, Yu et al. [125] have explained that NPs with diameter of 30 nm have induced ROS formation; but the NPs around 5 nm have not altered ROS content. The effect of size in toxicity of IONPs needs further investigation [115]. IO2 and IO3 exhibited redox-active iron ions (Fe^{2+}) that are capable of attacking cellular components; moreover, IO2 exerted the highest oxidative stress that might be attributed to their size that ranged between 5 and 7 nm. On the other side, IO1 exhibited (Fe^{3+}) with a size ranged from 20 to 25 nm; thereby, IO1 was involved in slight ROS generation. Moreover, there was no change in the general health of the rats exposed to IO1 throughout the study, thus demonstrate a safe toxicological profile that supports their use as potential nanotherapeutic agents.

In rats exposed to IO1, no significant alterations in hepatic and brain contents of oxidative stress markers or hepatic enzymes activity were observed, indicating that under the conditions IO1 do not cause deleterious hepatic or neural cell membrane damage. Taken together, the lack of significant biochemical alterations in IO1-exposed rats confirms that these particles do not affect the functional integrity of the liver or the brain. The altered redox defense status due to exposure of rats to IO1 might be described as an initial tissue response to the bioaccumulation of IONPs in the liver and brain. IO1 is well tolerated and does not affect the functional integrity of organs under study and thus suggests its potential biomedical application. Similarly, PG-8000-coated ultra-small superparamagnetic IONPs had excellent biocompatibility with only slightly increased ALP, ALT, and lipid peroxidation levels unaccompanied by any obvious histopathological alterations [128]. In addition, IONPs could effectively cross BBB; this iron transport in different organs could be achieved through the transferrin receptor [74]. This slight increase in brain IO1 level did not induce behavioral alterations in IO1-exposed rats, indicating no significant neurotoxic effects of these NPs.

The aforementioned biochemical investigation was supported by the electron TEM examination of both the liver and brain. It was demonstrated that histopathological investigation might fail to show structural alterations in organs exposed to repeated doses of IONPs [100]. For instance, the ultrastructural mitochondrial alterations in brains (neuropil) exposed to IO2 and IO3 as swollen cristolysed mitochondria or elongated mitochondria might be explained by a similar study of Skalska et al. [129] on silver NPs. Elongated mitochondria indicated that the stress of exposure to IONPs enhanced fusion activity [130]. This mitochondrial dysfunction might promote oxidative stress and enhance generation of free radicals. Ultrastructural evaluation by TEM revealed that IO1 administration did not stimulate any significant pathological damage upon comparison to normal control rats. In addition, the ultrastructural evaluation results are in

accordance with the other findings, which reveal that there is no significant alteration of hepatic tissues in IO1-exposed rats, as compared to control. According to our findings, IO1 shows less toxic properties as compared to IO2 and IO3.

Due to their high detection limit, ICP-OES is regarded as a “gold standard” approach to quantify IONPs; ICP-OES is of great importance in distribution studies as it can quantify iron without any additional labeling at a concentration of 0.1 mg/L (0.1 ppm) [131]. ICP-OES is utilized to quantify the cellular uptake and biodistribution of IONPs in rat liver and left brain, relative to control. Hydrodynamic size (hD) of the IONPs is one of the most important factors that controls biodistribution kinetics [132]. Reddy et al. [94] demonstrated that IONPs were absorbed and extensively deposited in the liver and the brain, using ICP-OES analysis. Similarly, Wang et al. [133] reported that deposition of IONPs in major systemic organs of mice at an oral dose of 600 mg/kg bwt is in support of our results. It was demonstrated that size and charge of NPs also affect the uptake and clearance mechanisms [94]. Hepatic accumulated IONPs is generally degraded into ionic Fe forms and released in the blood where it is conjugated with hemoglobin of erythrocytes and different iron-binding proteins [105]. On the other side, NPs can diffuse in the brain through pathways of rapid perivascular flow of cerebrospinal fluid (CSF) and slow axonal transport both anterograde and retrograde [134, 135].

The total Fe content and distribution of IONP-exposed liver and brains run in accordance with size of NPs of different formulations of IONPs, and IO2 with a size of 5–7 nm was highly accumulated in the brain (46.51%) due to their ability to cross BBB. While IO3 demonstrated the highest deposited Fe content in the liver (83.71%) and the lowest Fe content in the brain (35.04%), this distribution of Fe is strongly connected to the large size of NPs (32–40 nm) that trapped them in the liver tissue and hindered them from crossing BBB and subsequent deposition in the brain. This deposition of IONPs was evident by ultrastructural investigation of hepatocytes that showed clusters of NPs dispersed intracellular and extracellular. Regarding IO1, this formulation demonstrated an average distribution of Fe content in both liver and brain tissues, considering the average size of these NPs (20–25 nm). In addition, this manner of Fe distribution was supported by the least oxidative stress provoked by this formulation of IONPs. This runs in accordance with Kwon et al. [136] who performed an inhalation exposure study in mice that demonstrated that IONPs < 50 nm reached the brain without stimulating any side effects. It was revealed that uptake of IONPs was more in the liver and the brain; this organ distribution pattern is likely to be affected by Fe-binding proteins that act as Fe carriers (*e.g.*, transferrin and ferritin). Elevated Fe brain content might be ascribed to binding of Fe to transferrin that enhances the upregulation of Fe receptors in the brain thus delivering Fe across BBB

Table 5 Pattern of nanotoxicity of IONPs formulations

IONPs	Shape	Size (nm)	Iron ion	Toxicological profile
Chloride	Semi-spheres	19 ± 4.0	Fe ⁺³	Safe
Lactate	Semi-spheres	32 ± 3.0	Fe ⁺²	Toxic +
Nitrate	Semi-spheres	5 ± 2.0	Fe ⁺²	Toxic + +

[137]. Higher hepatic deposition and localization of IONPs might have triggered ultrastructural alterations. Comparison summary for nanotoxicity of the IONPs is illustrated in Table 5.

Conclusions

This study demonstrated that IO2 (IONPs-(NO₃)₃) was the most acutely toxic compound, followed by IO3 (IONPs-lactate), where IO1 (IONPs-Cl₃) exhibited a safe toxicological profile, which was explained by their different microstructures and physicochemical and surface area features. The oxidative stress-induced nanotoxicity was in the order of IO1 < IO3 < IO2. The biochemical investigations and the TEM examination suggested that the IO1 could be further used for developing novel nanotherapeutic applications including drug delivery to treat neurodegenerative disorders or liver diseases. Therefore, further kinetic and toxicokinetic investigations are essential to extend the current knowledge on NP behavior in vivo. Moreover, the results of this study provided useful information for risk analysis to define “safety limits” for the employment of IONPs in biomedical “nanotheranostic” applications by administrative agencies. This work is encouraging for further study on employing magnetic IONPs-chloride (IO1), as a nanotherapeutic agent, for efficient drug loading and delivery to manage neurodegenerative or liver disorders.

Author Contribution Dr. Ghadha Ibrahim Fouad and Dr. Mostafa Mabrouk: equally contributed to conceptualization, methodology, investigation, formal analysis, writing-original draft, and preparation. Dr. Sara A.M. El-Sayed: methodology, investigation, formal analysis. Prof. Dr. Maha Z. Rizk and Prof. Dr. Hanan H. Beherei: review and editing of the paper.

Funding This work was supported by the National Research Centre (NRC), Egypt (Project no.: 12060106, 2019–2021); P.I.: Dr. Ghadha Ibrahim Fouad).

Data availability All data generated or analyzed during this study are included in this published article.

Declarations

Ethics Approval The animal protocol was adopted in accordance with the National Research Council’s Guide for the Care and Use of Laboratory Animals (NIH Publications No. 8023, revised 1978), and experimental procedures were approved by the Ethical Committee, National Research Centre (NRC), Egypt (Approval no. 19–313).

Consent to Participate All authors gave their consent to participate in the present study.

Consent for Publication All authors gave approval to publish the present study.

Conflict of Interest The authors declare no competing interests.

References

- Aitken RJ, Creely KS, Tran CL (2004) Nanoparticles: an occupational hygiene review (41–44). HSE books, London
- Kataria S, Jain M, Rastogi A, Živčák M, Brestic M, Liu S, Tripathi DK (2019) Role of nanoparticles on photosynthesis: avenues and applications. In *Nanomaterials in plants, algae and microorganisms* (103–127). Academic Press.
- Mech A, Wohlleben W, Ghanem A, Hodoroaba VD, Weigel S, Babick F et al (2020) Nano or not nano? A structured approach for identifying nanomaterials according to the European Commission’s Definition. *Small* 16(36):2002228
- Jandt KD, Watts DC (2020) Nanotechnology in dentistry: Present and future perspectives on dental nanomaterials. *Dent Mater* 36(11):1365–1378. <https://doi.org/10.1016/j.dental.2020.08.006>
- Manzanares D, Ceña V (2020) Endocytosis: the nanoparticle and submicron nanocompounds gateway into the cell. *Pharmaceutics* 12(4):371
- Ibrahim Fouad G (2021) A proposed insight into the anti-viral potential of metallic nanoparticles against novel coronavirus disease-19 (COVID-19). *Bull Natl Res Cent* 45(1):1–22
- Vance ME, Kuiken T, Vejerano EP, McGinnis SP, Hochella Jr MF, Rejeski D, Hull MS (2015) Nanotechnology in the real world: redeveloping the nanomaterial consumer products inventory. *Beilstein J Nanotechnol* 6(1):1769–1780
- Mabrouk M, Das DB, Salem ZA, Beherei HH (2021) Nanomaterials for biomedical applications: production, characterisations, recent trends and difficulties. *Molecules* 26(4):1077
- Amanzadeh E, Esmaili A, Abadi RE, Kazemipour N, Pahlevaneshan Z, Beheshti S (2019) Quercetin conjugated with superparamagnetic iron oxide nanoparticles improves learning and memory better than free quercetin via interacting with proteins involved in LTP. *Sci Rep* 3 9(1) 1–9
- Misra R, Kandoi S, Varadaraj Vijayalakshmi S, Nanda A, Verma RS (2020) Nanotheranostics: a tactic for cancer stem cells prognosis and management. *J Drug Deliv Sci Technol* 55:101457
- Muthu MS, Leong DT, Mei L, Feng SS (2014) Nanotheranostics: application and further development of nanomedicine strategies for advanced theranostics. *Theranostics* 4(6):660
- Mura S, Couvreur P (2012) Nanotheranostics for personalized medicine. *Adv Drug Deliv Rev* 64(13):1394–1416
- Silva CO, Pinho JO, Lopes JM, Almeida AJ, Gaspar MM, Reis C (2019) Current trends in cancer nanotheranostics: metallic, polymeric, and lipid-based systems. *Pharmaceutics* 11(1):22

14. Misra R, Acharya S (2021) Smart nanotheranostic hydrogels for on-demand cancer management. *Drug Discov Today* 26(2):344–359. <https://doi.org/10.1016/j.drudis.2020.11.010>
15. Ferber S, Baabur-Cohen H, Blau R, Epshtein Y et al (2014) Polymeric nanotheranostics for real-time non-invasive optical imaging of breast cancer progression and drug release. *Cancer Lett* 352(1):81–89
16. Sifaka PI, Okur NÜ, Karantas ID, Okur ME, Gündođdu EA (2021) Current update on nanoplatforms as therapeutic and diagnostic tools: a review for the materials used as nanotheranostics and imaging modalities. *Asian J Pharm Sci* 16(1):24–46
17. Mahmoudi M, Hofmann H, Rothen-Rutishauser B, Petri-Fink A (2012) Assessing the *in vitro* and *in vivo* toxicity of superparamagnetic iron oxide nanoparticles. *Chem reviews* 112(4):2323–2338
18. Ibrahim Fouad G, Ahmed KA (2021) Neuroprotective potential of Berberine against doxorubicin-induced toxicity in rat's brain. *Neurochem Res*, 1–17.
19. Zhao Y, Fletcher NL, Liu T, Gemmell AC, Houston ZH, Blakey I, Thurecht KJ (2018) *In vivo* therapeutic evaluation of polymeric nanomedicines: effect of different targeting peptides on therapeutic efficacy against breast cancer. *Nanotheranostics* 2(4):360
20. Gupta AS (2011) Nanomedicine approaches in vascular disease: a review. *Nanomedicine* 7(6):763–779
21. Chen Q, Du Y, Zhang K, Liang Z, Li J, Yu H et al (2018) Tau-targeted multifunctional nanocomposite for combinational therapy of Alzheimer's disease. *ACS Nano* 12(2):1321–1338
22. Poljak-Blaži M, Jaganjac M, Žarković N (2010) Cell oxidative stress: risk of metal nanoparticles. In *Handbook of nanophysics nanomedicine and nanorobotic*; CRC Press: New York, NY, USA.
23. Li S, Jiang C, Wang H, Cong S, Tan M (2018) Fluorescent nanoparticles present in Coca-Cola and Pepsi-Cola: physicochemical properties, cytotoxicity, biodistribution and digestion studies. *Nanotoxicol* 12(1):49–62
24. Adeyemi OS, Adewumi I, Faniyan TO (2015) Silver nanoparticles influenced rat serum metabolites and tissue morphology. *JBCPP* 26(4):355–361. <https://doi.org/10.1515/jbcpp-2013-0092> (PMID: 25460283)
25. Elbially NS, Aboushoushah SF, Alshammari WW (2019) Long-term biodistribution and toxicity of curcumin capped iron oxide nanoparticles after single-dose administration in mice. *Life Sci* 1(230):76–83. <https://doi.org/10.1016/j.lfs.2019.05.048> (Epub 2019 May 22 PMID: 31128136)
26. Tomankova K, Horakova J, Harvanova M, Malina L, Soukupova J, Hradilova S et al (2015) Cytotoxicity, cell uptake and microscopic analysis of titanium dioxide and silver nanoparticles *in vitro*. *Food Chem Toxicol* 82:106–115
27. Gan J, Sun J, Chang X, Li W, Li J, Niu S et al (2020) Biodistribution and organ oxidative damage following 28 days oral administration of nanosilver with/without coating in mice. *J Appl Toxicol* 40(6):815–831
28. Yousef MI, Abuzreda AA, Kamel MA (2019) Cardiotoxicity and lung toxicity in male rats induced by long-term exposure to iron oxide and silver nanoparticles. *Exp Ther Med* 18:4329–4339. <https://doi.org/10.3892/etm.2019.8108>
29. Roda E, Bottone MG, Biggiogera M, Milanesi G, Coccini T (2019) Pulmonary and hepatic effects after low dose exposure to nanosilver: early and long-lasting histological and ultrastructural alterations in rat. *Toxicol rep* 6:1047–1060
30. Saptarshi SR, Duschl A, Lopata AL (2013) Interaction of nanoparticles with proteins: relation to bio-reactivity of the nanoparticle. *J Nanobiotechnol* 19(11):26. <https://doi.org/10.1186/1477-3155-11-26> (PMID:23870291;PMCID:PMC3720198)
31. Tsai MF, Hsu C, Yeh CS, Hsiao YJ, Su CH, Wang LF (2018) Tuning the distance of rattle-shaped IONP@ shell-in-shell nanoparticles for magnetically-targeted photothermal therapy in the second near-infrared window. *ACS Appl Mater interfaces* 10(2):1508–1519
32. Peng X, Chen H, Huang J, Mao H and Shin D M (2011) Targeted magnetic iron oxide nanoparticles for tumor imaging and therapy *Biomedical Engineering—From Theory to Applications* (Rijeka: InTech)
33. Jain TK, Reddy MK, Morales MA, Leslie-Pelecky DL, Labhassetwar V (2008) Biodistribution, clearance, and biocompatibility of iron oxide magnetic nanoparticles in rats. *Mol Pharm* 5(2):316–327
34. Nosrati H, Salehiabar M, Attari E, Davaran S, Danafar H, Manjili HK (2018) Green and one-pot surface coating of iron oxide magnetic nanoparticles with natural amino acids and biocompatibility investigation. *Appl Organomet Chem* 32(2):e4069
35. Nosrati H, Tarantash M, Bochani S, Charmi J, Bagheri Z, Fridoni M et al (2019) Glutathione (GSH) peptide conjugated magnetic nanoparticles as blood–brain barrier shuttle for mri-monitored brain delivery of paclitaxel. *ACS Biomater Sci Eng* 5(4):1677–1685
36. Ittrich H, Peldschus K, Raabe N, Kaul M, Adam G (2013) Superparamagnetic iron oxide nanoparticles in biomedicine: applications and developments in diagnostics and therapy. *Rofo* 185(12):1149–66. <https://doi.org/10.1055/s-0033-1335438> (Epub 2013 Sep 5. PMID: 24008761)
37. Lindemann A, Lüttke-Buzug K, Fräderich BM, Gräfe K, Pries R, Wollenberg B (2014) Biological impact of superparamagnetic iron oxide nanoparticles for magnetic particle imaging of head and neck cancer cells. *Int J Nanomedicine* 9:5025–40. <https://doi.org/10.2147/IJN.S63873> (PMID: 25378928; PMCID: PMC4218924)
38. Rosen JE, Chan L, Shieh DB, Gu FX (2012) Iron oxide nanoparticles for targeted cancer imaging and diagnostics. *Nanomedicine: NBM* 8(3):275–290
39. Mody VV, Cox A, Shah S, Singh A, Bevins W, Parihar H (2014) Magnetic nanoparticle drug delivery systems for targeting tumor. *ApplNanosci* 4:385–392
40. Dikpati A, Madgulkar AR, Kshirsagar SJ, Bhalekar MR, Chahal AS (2012) Targeted drug delivery to CNS using nanoparticles. *JAPS* 2(1):179–191
41. Albanese A, Tang PS, Chan WC (2012) The effect of nanoparticle size, shape, and surface chemistry on biological systems. *Annu Rev Biomed Eng* 14:1–16
42. Zhu M, Diao G (2011) Synthesis of porous Fe₃O₄ nanospheres and its application for the catalytic degradation of xylene orange. *Am J Phys Chem C* 115(39):18923–18934
43. Hyeon T (2003) Chemical synthesis of magnetic nanoparticles. *ChemComm* 8:927–934
44. Huang C, Zhang H, Sun Z, Zhao Y, Chen S, Tao R, Liu Z (2011) Porous Fe₃O₄ nanoparticles: synthesis and application in catalyzing epoxidation of styrene. *J Colloid Interface Sci* 364(2):298–303
45. Alkilany AM, Murphy CJ (2010) Toxicity and cellular uptake of gold nanoparticles: what we have learned so far? *J Nanopart Res* 12(7):2313–2333
46. Lei L, Ling-Ling J, Yun Z, Gang L (2013) Toxicity of superparamagnetic iron oxide nanoparticles: research strategies and implications for nanomedicine. *Chin Phys B* 22:1–10
47. Voliani V, Signore G, Nifosi R, Ricci F, Luin S, Beltram F (2012) Smart delivery and controlled drug release with gold nanoparticles: new frontiers in nanomedicine. *Recent Pat Nanotechnol* 2(1):34–44

48. Prabhakar P, Vijayaraghavan S, Philip J, Doble M (2011) Biocompatibility studies of functionalized CoFe₂O₄ magnetic nanoparticles. *Curr Nanosci* 7(3):371–376
49. Damoiseaux R, George S, Li M, Pokhrel S, Ji Z, France B et al (2011) No time to lose—high throughput screening to assess nanomaterial safety. *Nanoscale* 3(4):1345–1360
50. Jeng HA, Swanson J (2006) Toxicity of metal oxide nanoparticles in mammalian cells. *J Environ Sci Health A* 41(12):2699–2711
51. Valdiglesias V, Fernández-Bertólez N, Kiliç G, Costa C, Costa S, Fraga S et al (2016) Are iron oxide nanoparticles safe? Current knowledge and future perspectives. *J Trace Elem Med Biol* 38:53–63
52. El-Boubbou K (2018) Magnetic iron oxide nanoparticles as drug carriers: clinical relevance. *Nanomed* 13(8):953–971. <https://doi.org/10.2217/nnm-2017-0336> (Epub 2018 Jan 29 PMID: 29376469)
53. Wu J, Ding T, Sun J (2013) Neurotoxic potential of iron oxide nanoparticles in the rat brain striatum and hippocampus. *Neurotoxicol* 34:243–253
54. Glat M, Skaat H, Menkes-Caspi N, Margel S, Stern EA (2013) Age-dependent effects of microglial inhibition *in vivo* on Alzheimer's disease neuropathology using bioactive-conjugated iron oxide nanoparticles. *J Nanobiotechnol* 11(32):1–12
55. Poduslo JF, Hultman KL, Curran GL, Preboske GM, Chamberlain R (2011) Targeting vascular amyloid in arterioles of Alzheimer disease transgenic mice with amyloid beta protein antibody-coated nanoparticles. *Neuropathol Exp Neurol* 70(653–61):4
56. Naumenko V, Garanina A, Nikitin A, Vodopyanov S, Vorobyeva N et al (2018) Biodistribution and tumors MRI contrast enhancement of magnetic nanocubes, nanoclusters, and nanorods in multiple mice models. *CONTRAST MEDIA MOL I*:2018
57. Paik SYR, Kim JS, Shin SJ, Ko S (2015) Characterization, quantification, and determination of the toxicity of iron oxide nanoparticles to the bone marrow cells. *Int J Mol Sci* 16(9):22243–22257
58. Mohamed MI, Mohammad MK, Abdul Razak HR, Abdul Razak K, Saad WM (2015) Nanotoxic profiling of novel iron oxide nanoparticles functionalized with perchloric acid and SiPEG as a radiographic contrast medium. *Biomed Res Int* 2015:183525. <https://doi.org/10.1155/2015/183525> (Epub May 17. PMID: 26075217; PMCID: PMC4449877)
59. Xiong F, Wang H, Feng Y, Li Y, Hua X, Pang X, Zhang S, Song L, Zhang Y, Gu N (2015) Cardioprotective activity of iron oxide nanoparticles. *Sci Rep* 5:8579. <https://doi.org/10.1038/srep08579> (PMID:25716309;PMCID:PMC4341209)
60. Dhakshinamoorthy V, Manickam V, Perumal E (2017) Neurobehavioural toxicity of iron oxide nanoparticles in mice. *Neurotox Res* 32(2):187–203. <https://doi.org/10.1007/s12640-017-9721-1> (Epub 2017 Mar 20. PMID: 28321581)
61. Valdiglesias V, Kiliç G, Costa C, Fernández-Bertólez N, Pásaro E, Teixeira JP et al (2015) Effects of iron oxide nanoparticles: cytotoxicity, genotoxicity, developmental toxicity, and neurotoxicity. *Environ Mol Mutagen* 56(2):125–148
62. Vinzant N, Scholl JL, Wu C-M, Kindle T, Koodali R, Forster GL (2017) Iron oxide nanoparticle delivery of peptides to the brain: reversal of anxiety during drug withdrawal. *Front Neurosci* 11:608
63. Shaker S, Zafarian S, Chakra CS, Rao KV (2013) Preparation and characterization of magnetite nanoparticles by Sol-Gel method for water treatment. *Int J Innov Res Sci Eng Technol* 2(7):2969–2973
64. OECD Guidelines for the testing of chemicals: acute oral toxicity—fixed dose procedure, OECD/OCDE 420. Adopted: 17th December 2001.
65. Najafabadi RE, Kazemipour N, Esmaeili A, Beheshti S, Nazifi S (2018) Using superparamagnetic iron oxide nanoparticles to enhance bioavailability of quercetin in the intact rat brain. *BMC Pharmacol Toxicol* 19(1):1–12
66. Askri D, Ouni S, Galai S, Chovelon B, Arnaud J, Sturm N et al (2019) Nanoparticles in foods? A multiscalephysiopathological investigation of iron oxide nanoparticle effects on rats after an acute oral exposure: Trace element biodistribution and cognitive capacities. *Food Chem Toxicol* 127:173–181
67. Reitman A, Frankel SA (1957) colorimetric method for the determination of serum glutamic oxalacetic and glutamic pyruvic transaminases. *Am J ClinPathol* 28(1):56–63. <https://doi.org/10.1093/ajcp/28.1.56> (PMID: 13458125)
68. Belfield A, Goldberg DM (1971) Revised assay for serum phenyl phosphatase activity using 4-amino-antipyrine. *Enzyme* 12(5):561–573. <https://doi.org/10.1159/000459586> (PMID: 5169852)
69. Ohkawa H, Ohishi N, Yagi K (1979) Assay for lipid peroxides in animal tissues by thiobarbituric acid reaction. *Anal Biochem* 95(2):351–358
70. Beutler E, Duron O, Kelly BM (1963) Improved method for the determination of blood glutathione. *J Lab Clin Med* 61:882–888 (PMID: 13967893)
71. Aebi H (1984) Catalase *in vitro*. *Methods Enzymol* 105:121–126
72. American Public Health Association (APHA), American Water Works Association (AWWA), and Water Environment Federation (WEF) 2017. Standard Methods for the Examination of Water and Wastewater, 23rd ed. (Rice, E. W., Baird, R. B., Eaton, A. D., Clesceri, L. S. eds.) Washington DC.
73. Gaharwar US, Meena R, Rajamani P (2017) Iron oxide nanoparticles induced cytotoxicity, oxidative stress and DNA damage in lymphocytes. *J Appl Toxicol* 37:1232–1244. <https://doi.org/10.1002/jat.3485>
74. Xu YY, Zhao D, Zhang XJ, Jin WT, Kashkarov P, Zhang H (2009) Synthesis and characterization of single-crystalline α -Fe₂O₃ nanoleaves. *Physica E Low Dimens Syst Nanostruct* 41(5):806–811
75. Labani MM et al (2013) Evaluation of pore size spectrum of gas shale reservoirs using low pressure nitrogen adsorption, gas expansion and mercury porosimetry: a case study from the Perth and Canning Basins, Western Australia. *J Pet Sci Eng* 112:7–16
76. Fudimura KA, Seabra AB, Santos MC, Haddad PS (2017) Synthesis and characterization of methylene blue-containing silica-coated magnetic nanoparticles for photodynamic therapy. *J Nanosci Nanotechnol* 17(1):133–142
77. Santos MC, Seabra AB, Pelegrino MT, Haddad PS (2016) Synthesis, characterization and cytotoxicity of glutathione-and PEG-glutathione-superparamagnetic iron oxide nanoparticles for nitric oxide delivery. *App Surface Scie* 367:26–35
78. Molina MM, Seabra AB, de Oliveira MG, Itri R, Haddad PS (2013) Nitric oxide donor superparamagnetic iron oxide nanoparticles. *Mater Sci Eng C* 33(2):746–751
79. Gonçalves LC, Seabra AB, Pelegrino MT, De Araujo DR, Bernardes JS, Haddad PS (2017) Superparamagnetic iron oxide nanoparticles dispersed in Pluronic F127 hydrogel: potential uses in topical applications. *RSC Adv* 7(24):14496–14503
80. Dorniani D, Hussein MZB, Kura AU, Fakurazi S, Shaari AH, Ahmad Z (2013) Sustained release of prindopril erbumine from its chitosan-coated magnetic nanoparticles for biomedical applications. *Int J Mol Sci* 14(12):23639–23653
81. Rufus A, Sreeju N, Philip D (2016) Synthesis of biogenic hematite (α -Fe₂O₃) nanoparticles for antibacterial and nanofluid applications. *RSC Adv* 6(96):94206–94217
82. Li Q, Kartikowati CW, Horie S, Ogi T, Iwaki T, Okuyama K (2017) Correlation between particle size/domain structure and

- magnetic properties of highly crystalline Fe₃O₄ nanoparticles. *Scien rep* 7(1):1–7
83. Bodade AB, Taiwade MA, Chaudhari GN (2017) Bioelectrode based chitosan-nanocopperoxide for application to lipase biosensor. *J Appl Pharm Res* 5:30–39
 84. Kumar KN, Padma R, Ratnakaram YC, Kang M (2017) Bright green emission from f-MWCNT embedded co-doped Bi³⁺+Tb³⁺: polyvinyl alcohol polymer nanocomposites for photonic applications. *RSC Adv* 7:15084–15095
 85. Sivakumar M, Gedanken A, Zhong W, Jiang YH, Du YW, Bruckental I et al (2004) Sonochemical synthesis of nanocrystalline LaFeO₃. *J Mater Chem* 14(4):764–769
 86. Kumar P, Rawat N, Hang DR, Lee HN, Kumar R (2015) Controlling band gap and refractive index in dopant-free α-Fe₂O₃ films. *Electron Mater Lett* 11(1):13–23
 87. Prozorov R, Yeshurun Y, Prozorov T, Gedanken A (1999) Magnetic irreversibility and relaxation in assembly of ferromagnetic nanoparticles. *Phys Rev B* 59(10):6956
 88. Ashour MM, Mabrouk M, Soliman IE, Beherei HH, Tohamy KM (2021) Mesoporous silica nanoparticles prepared by different methods for biomedical applications: Comparative study. *IET Nanobiotechnol* 15(3):291–300
 89. Mabrouk M, Abd El-Wahab RM, Beherei HH, Selim MM, Das DB (2020) Multifunctional magnetite nanoparticles for drug delivery: preparation, characterization, antibacterial properties and drug release kinetics. *Int J Pharm* 587:119658
 90. Brohi RD, Wang L, Talpur HS, Wu D, Khan FA, Bhattarai D et al (2017) Toxicity of nanoparticles on the reproductive system in animal models: a review. *Front pharmacol* 8:606
 91. Kumar A, Pandey AK, Singh SS, Shanker R, Dhawan A (2011) Cellular uptake and mutagenic potential of metal oxide nanoparticles in bacterial cells. *Chemosphere* 83:1124–1132
 92. Feng Q, Liu Y, Huang J, Chen K, Huang J, Xiao K (2018) Uptake, distribution, clearance, and toxicity of iron oxide nanoparticles with different sizes and coatings. *Scien rep* 8(1):1–13
 93. Hayes AW, Kruger CL (Eds.) (2014) *Hayes' principles and methods of toxicology*. Crc Press.
 94. Reddy UA, Prabhakar PV, Mahboob M (2017) Biomarkers of oxidative stress for *in vivo* assessment of toxicological effects of iron oxide nanoparticles. *Saudi J Biol Sci* 24(6):1172–1180
 95. Bugata LSP, Pitta Venkata P, Gundu AR, Mohammed Fazlur R, Reddy UA, Kumar JM et al (2019) Acute and subacute oral toxicity of copper oxide nanoparticles in female albino Wistar rats. *J Appl Toxicol* 39(5):702–716
 96. Bertrand N, Wu J, Xu X, Kamaly N, Farokhzad OC (2014) Cancer nanotechnology: the impact of passive and active targeting in the era of modern cancer biology. *Adv Drug Deliv Rev* 66:2–25
 97. Almeida JPM, Chen AL, Foster A, Drezek R (2011) *In vivo* biodistribution of nanoparticles. *Nanomed* 6(5):815–835
 98. Van Rooy I, Cakir-Tascioglu S, Hennink WE, Storm G, Schiffelers RM, Mastrobattista E (2011) *In vivo* methods to study uptake of nanoparticles into the brain. *Pharm res* 28(3):456–471
 99. Adeyemi OS, Sulaiman FA (2012) Biochemical and morphological changes in Trypanosomabrucei-brucei-infected rats treated with homidium chloride and diminazeneaceturate. *JBCPP* 23(4):179–183
 100. Kumari M, Rajak S, Singh SP, Murty US, Mahboob M, Grover P, Rahman MF (2013) Biochemical alterations induced by acute oral doses of iron oxide nanoparticles in Wistar rats. *Drug chem toxicol* 36(3):296–305. <https://doi.org/10.3109/01480545.2012.720988> (Epub 2012 Oct 1 PMID: 23025823)
 101. Sadauskas E, Wallin H, Stoltenberg M, Vogel U, Doering P, Larsen A, Danscher G (2007) Kupffer cells are central in the removal of nanoparticles from the organism. *Particle fibre toxicol* 4(1):1–7
 102. Lynch ED, Gu R, Pierce C, Kil J (2005) Combined oral delivery of ebselen and allopurinol reduces multiple cisplatin toxicities in rat breast and ovarian cancer models while enhancing anti-tumor activity. *Anticancer Drugs* 16(5):569–579
 103. Blanco E, Shen H, Ferrari M (2015) Principles of nanoparticle design for overcoming biological barriers to drug delivery. *Nature biotech* 33(9):941–951. <https://doi.org/10.1038/nbt.3330>
 104. Montalbetti N, Simonin A, Kovacs G, Hediger MA (2013) Mammalian iron transporters: families SLC11 and SLC40. *Mol Aspects Med* 34(2–3):270–287
 105. Easo SL, Mohanan PV (2016) Hepatotoxicity evaluation of dextran stabilized iron oxide nanoparticles in Wistar rats. *Int J Pharm* 509(1–2):28–34
 106. Shirband A et al (2014) Dose-dependent effects of iron oxide nanoparticles on thyroid hormone concentrations in liver enzymes: possible tissue destruction. *Global J Med Res Studies* 1(1):28–31
 107. Kaplan MM (1972) Alkaline phosphatase. *N Engl J Med* 286(4):200–202
 108. Askri D, Cunin V, Ouni S, Béal D, Rachidi W, Sakly M et al (2019) Effects of iron oxide nanoparticles (γ-Fe₂O₃) on liver, lung and brain proteomes following sub-acute intranasal exposure: a new toxicological assessment in rat model using iTRAQ-based quantitative proteomics. *Int J Mol Sci* 20(20):5186
 109. Giannini EG, Testa R, Savarino V (2005) Liver enzyme alteration: a guide for clinicians. *CMAJ* 172(3):367–379
 110. Hare D, Ayton S, Bush A, Lei P (2013) A delicate balance: iron metabolism and diseases of the brain. *Front Aging Neurosci* 18(5):34. <https://doi.org/10.3389/fnagi.2013.00034> (PMID:23874300;PMCID:PMC3715022)
 111. Ward RJ, Zucca FA, Duyn JH, Crichton RR, Zecca L (2014) The role of iron in brain ageing and neurodegenerative disorders. *Lancet Neurol* 13(10):1045–1060. [https://doi.org/10.1016/S1474-4422\(14\)70117-6](https://doi.org/10.1016/S1474-4422(14)70117-6) (PMID:25231526;PMCID:PMC5672917)
 112. Chen P, Totten M, Zhang Z, Bucinca H, Erikson K, Santamaria A, Aschner Bowman AB, M, (2019) Iron and manganese-related CNS toxicity: mechanisms, diagnosis and treatment. *Expert Rev Neurother* 19(3):243–260. <https://doi.org/10.1080/14737175.2019.1581608>
 113. Borai IH, Ezz MK, Rizk MZ, Aly HF, El-Sherbiny M, Matloub AA, Fouad GI (2017) Therapeutic impact of grape leaves polyphenols on certain biochemical and neurological markers in Aβ1-3-induced Alzheimer's disease. *Biomed Pharmacother* 93:837–851. <https://doi.org/10.1016/j.biopha.2017.07.038> (Epub 2017 Jul 14. PMID: 28715867)
 114. Sripetchwande J, Wongjaikam S, Krinratun W, Chattipakorn N, Chattipakorn SC (2016) A combination of an iron chelator with an antioxidant effectively diminishes the dendritic loss, tau-hyperphosphorylation, amyloids-β accumulation and brain mitochondrial dynamic disruption in rats with chronic iron-overload. *Neurosci* 332:191–202
 115. Yarjanli Z, Ghaedi K, Esmaeili A, Rahgozar S, Zarrabi A (2017) Iron oxide nanoparticles may damage to the neural tissue through iron accumulation, oxidative stress, and protein aggregation. *BMC Neurosci* 18(1):51. <https://doi.org/10.1186/s12868-017-0369-9>
 116. Sun L, Li Y, Liu X, Jin M, Zhang L, Du Z et al (2011) Cytotoxicity and mitochondrial damage caused by silica nanoparticles. *Toxicol in vitro* 25(8):1619–1629
 117. Lee HP, Zhu X, Liu G, Chen SG, Perry G, Smith MA et al (2010) Divalent metal transporter, iron, and Parkinson's disease: a pathological relationship. *Cell Res* 20:397–399
 118. Cortajarena AL, Ortega D, Ocampo SM, Gonzalez-García A, Couleaud P, Miranda, R, et al. (2014) Engineering iron oxide

- nanoparticles for clinical settings. *Nanobiomed* 1(Godište 2014), 1–2]
119. Fu PP, Xia Q, Hwang HM, Ray PC, Yu H (2014) Mechanisms of nanotoxicity: generation of reactive oxygen species. *J Food Drug Anal* 22(1):64–75
 120. Liu Y, Li J, Xu K et al (2018) Characterization of superparamagnetic iron oxide nanoparticle-induced apoptosis in PC12 cells and mouse hippocampus and striatum. *Toxicol Lett* 292:151–161
 121. Barbusinski K (2009) Fenton reaction-controversy concerning the chemistry. *Bioorg Chem* 16:347–358
 122. Mantzaris MD, Bellou S, Skiada V, Kitsati N, Fotsis T, Galaris D (2016) Intracellular labile iron determines H₂O₂-induced apoptotic signaling via sustained activation of ASK1/JNK-p38 axis. *Free Radic Biol Med* 97:454–465
 123. Núñez MT, Urrutia P, Mena N, Aguirre P, Tapia V, Salazar J (2012) Iron toxicity in neurodegeneration. *Biometals* 25:761–776
 124. Farshbaf MJ, Ghaedi K (2016) Does any drug to treat cancer target mTOR and iron hemostasis in neurodegenerative disorders? *Biometals*. <https://doi.org/10.1007/s10534-016-9981-x>
 125. Yu M, Huang S, Yu KJ, Clyne AM (2012) Dextran and polymer polyethylene glycol (PEG) coating reduce both 5 and 30 nm iron oxide nanoparticle cytotoxicity in 2D and 3D cell culture. *Int J Mol Sci* 13(5):5554–5570
 126. Zhu L, Zhou Z, Mao H, Yang L (2017) Magnetic nanoparticles for precision oncology: theranostic magnetic iron oxide nanoparticles for image-guided and targeted cancer therapy. *Nanomed* 12(1):73–87
 127. Imam SZ, Lantz-McPeak SM, Cuevas E, Rosas-Hernandez H, Liachenko S, Zhang Y et al (2015) Iron oxide nanoparticles induce dopaminergic damage: *in vitro* pathways and *in vivo* imaging reveals mechanism of neuronal damage. *Mol Neurobiol* 52:913–926
 128. Rajan B, Sathish S, Balakumar S, Devaki T (2015) Synthesis and dose interval dependent hepatotoxicity evaluation of intravenously administered polyethylene glycol-8000 coated ultra-small superparamagnetic iron oxide nanoparticle on Wistar rats. *Environ Toxicol Pharmacol* 39(2):727–735
 129. Skalska J, Dąbrowska-Bouta B, Frontczak-Baniewicz M et al (2020) A low dose of nanoparticulate silver induces mitochondrial dysfunction and autophagy in adult rat brain. *Neurotox Res* 38:650–664. <https://doi.org/10.1007/s12640-020-00239-4>
 130. Gomes LC, Di Benedetto G, Scorrano L (2011) During autophagy mitochondria elongate, are spared from degradation and sustain cell viability. *Nat Cell Biol* 13:589–598
 131. Patil US, Adireddy S, Jaiswal A, Mandava S, Chrisey LBR, DB, (2015) *In vitro/in vivo* toxicity evaluation and quantification of iron oxide nanoparticles. *Int J Mol Sci* 16(10):24417–24450
 132. Yang L, Kuang H, Zhang W, Aguilar ZP, Xiong Y, Lai W, Xu H, Wei H (2015) Size dependent biodistribution and toxicokinetics of iron oxide magnetic nanoparticles in mice. *Nanoscale* 7(2):625–636. <https://doi.org/10.1039/c4nr05061d> (PMID: 25423473)
 133. Wang J, Chen Y, Chen B, Ding J, Xia G, Gao C et al (2010) Pharmacokinetic parameters and tissue distribution of magnetic Fe₃O₄ nanoparticles in mice. *Int J nanomed* 5:861
 134. Su L, Zhang B, Huang Y, Zhang H, Xu Q, Tan J (2017) Superparamagnetic iron oxide nanoparticles modified with dimyristoylphosphatidylcholine and their distribution in the brain after injection in the rat substantia nigra. *Mater Sci Eng C* 81:400–406
 135. Yokel R, Grulke E, MacPhail R (2013) Metal-based nanoparticle interactions with the nervous system: the challenge of brain entry and the risk of retention in the organism. *Wiley Interdiscip Rev Nanomed Nanobiotechnol WIREs NANOMED NANOBIO* 5(4):346–373
 136. Kwon JT, Hwang SK, Jin H, Kim DS et al (2008) Body distribution of inhaled fluorescent magnetic nanoparticles in the mice. *J Occup Health* 50(1):1–6
 137. Descamps L, Dehouck MP, Torpier G, Cecchelli R (1996) Receptor-mediated transcytosis of transferrin through blood-brain barrier endothelial cells. *Am J Physiol-Heart C* 270(4):H1149–H1158
- Publisher's Note** Springer Nature remains neutral with regard to jurisdictional claims in published maps and institutional affiliations.